Draft version September 10, 2026
Typeset using LaTeX **twocolumn** style in AASTeX7.0.1

SHELLQs. Black Hole Mass and Eddington Ratio Distributions of Intermediate-Luminosity Quasars at $6 < z < 7$

Masafusa Onoue,[1,2] John D. Silverman,[2,3,4,5] Yoshiki Matsuoka,[6] Xuheng Ding,[7] Camryn L. Phillips,[8] Michael A. Strauss,[8] Junya Arita,[3] Takuma Izumi,[9,10,11,12] Mahoshi Sawamura,[10,9] Nobunari Kashikawa,[3,13] Irham Andika,[14] Kentaro Aoki,[15] Shunsuke Baba,[16] Anna-Christina Eilers,[17] Seiji Fujimoto,[18,19] Tomotsugu Goto,[20,21] Masatoshi Imanishi,[9,11] Kohei Inayoshi,[22] Kazushi Iwasawa,[23,24] Knud Jahnke,[25] Yuki Kaneko,[26] Toshihiro Kawaguchi,[27] Kotaro Kohno,[28,13] Chien-Hsiu Lee,[29] Alessandro Lupi,[30,31] Tohru Nagao,[32,12] Dragan Salak,[33] Malte Schramm,[34] Yoshiki Toba,[35,36,6] Hideki Umehata,[37] Marta Volonteri,[38] Fabian Walter,[25] Feige Wang,[39] and Jinyi Yang[39]

[1] *Waseda Institute for Advanced Study (WIAS), Waseda University, 1-21-1, Nishi-Waseda, Shinjuku, Tokyo 169-0051, Japan*
[2] *Kavli Institute for the Physics and Mathematics of the Universe (Kavli IPMU, WPI), UTIAS, Tokyo Institutes for Advanced Study, University of Tokyo, Chiba, 277-8583, Japan*
[3] *Department of Astronomy, School of Science, The University of Tokyo, 7-3-1 Hongo, Bunkyo-ku, Tokyo 113-0033, Japan*
[4] *Center for Data-Driven Discovery, Kavli IPMU (WPI), UTIAS, The University of Tokyo, Kashiwa, Chiba 277-8583, Japan*
[5] *Center for Astrophysical Sciences, Department of Physics & Astronomy, Johns Hopkins University, Baltimore, MD 21218, USA*
[6] *Research Center for Space and Cosmic Evolution, Ehime University, Matsuyama, Ehime 790-8577, Japan*
[7] *School of Physics and Technology, Wuhan University, Wuhan 430072, China*
[8] *Department of Astrophysical Sciences, Princeton University, 4 Ivy Lane, Princeton, NJ 08544, USA*
[9] *National Astronomical Observatory of Japan, National Institutes of Natural Sciences, 2-21-1 Osawa, Mitaka, Tokyo 181-8588, Japan*
[10] *Department of Astronomy, The University of Tokyo, 7-3-1 Hongo, Bunkyo, Tokyo 113-0033, Japan*
[11] *Department of Astronomy, School of Science, Graduate University for Advanced Studies (SOKENDAI), Mitaka, Tokyo 181-8588, Japan*
[12] *Amanogawa Galaxy Astronomy Research Center, Kagoshima University, 1-21-35 Korimoto, Kagoshima 890-0065, Japan*
[13] *Research Center for the Early Universe, Graduate School of Science, The University of Tokyo, 7-3-1 Hongo, Bunkyo-ku, Tokyo 113-0033, Japan*
[14] *Universitäts-Sternwarte München, Fakultät für Physik, Ludwig-Maximilians-Universität München, Scheinerstr. 1, 81679 München, Germany*
[15] *Subaru Telescope, National Astronomical Observatory of Japan, 650 North A'ohoku Place, Hilo HI 96720 U.S.A.*
[16] *Institute of Space and Astronautical Science (ISAS), Japan Aerospace Exploration Agency (JAXA), 3-1-1 Yoshinodai, Chuo-ku, Sagamihara, Kanagawa 252-5210, Japan*
[17] *MIT Kavli Institute for Astrophysics and Space Research, Massachusetts Institute of Technology, Cambridge, MA 02139, USA*
[18] *David A. Dunlap Department of Astronomy and Astrophysics, University of Toronto, 50 St. George Street, Toronto, Ontario, M5S 3H4, Canada*
[19] *Dunlap Institute for Astronomy and Astrophysics, 50 St. George Street, Toronto, Ontario, M5S 3H4, Canada*
[20] *Department of Physics, National Tsing Hua University, 101, Section 2. Kuang-Fu Road, Hsinchu, 30013, Taiwan*
[21] *Institute of Astronomy, National Tsing Hua University, 101, Section 2. Kuang-Fu Road, Hsinchu, 30013, Taiwan*
[22] *Kavli Institute for Astronomy and Astrophysics, Peking University, Beijing 100871, People's Republic of China*
[23] *Institut de Ciències del Cosmos (ICCUB), Universitat de Barcelona (IEEC-UB), Martí i Franquès, 1, 08028 Barcelona, Spain*
[24] *ICREA, Pg Lluís Companys 23, 08010 Barcelona, Spain*
[25] *Max Planck Institute for Astronomy, Königstuhl 17, 69117 Heidelberg, Germany*
[26] *Graduate School of Advanced Science and Engineering, Waseda University, Nishi-Waseda Campus, Waseda University, 3-4-1 Okubo, Shinjuku-ku, Tokyo 1699-8555 Japan*
[27] *Graduate School of Science and Engineering, University of Toyama, Gofuku 3190, Toyama 930-8555, Japan*
[28] *Institute of Astronomy, Graduate School of Science, The University of Tokyo, 2-21-1 Osawa, Mitaka, Tokyo 181-0015, Japan*
[29] *Hobby-Eberly Telescope, McDonald Observatory, The University of Texas at Austin, Fort Davis, TX 79734, USA*
[30] *Como Lake Center for Astrophysics, DiSAT, Università degli Studi dell'Insubria, via Valleggio 11, I-22100 Como, Italy*
[31] *INFN, Sezione di Milano-Bicocca, Piazza della Scienza 3, 20126 Milano, Italy*
[32] *Research Center for Space and Cosmic Evolution, Ehime University, 2-5 Bunkyo-cho, Matsuyama, Ehime 790-8577, Japan*
[33] *Astronomical Institute, Tohoku University, 6-3 Aramaki, Aoba-ku, Sendai, Miyagi 980-8578, Japan*
[34] *Universität Potsdam, Karl-Liebknecht-Straße 24/25, D-14476 Potsdam, Germany*
[35] *Department of Physical Sciences, Ritsumeikan University, 1-1-1 Noji-higashi, Kusatsu, Shiga 525-8577, Japan*

Corresponding author: Masafusa Onoue
masafusa.onoue@aoni.waseda.jp

[36] Academia Sinica Institute of Astronomy and Astrophysics, 11F of Astronomy-Mathematics Building, AS/NTU, No. 1, Section 4, Roosevelt Road, Taipei 10617, Taiwan
[37] Institute for Advanced Research, Nagoya University, Furocho, Chikusa, Nagoya 464-8602, Japan
[38] Institut d'Astrophysique de Paris, UMR 7095, CNRS and Sorbonne Université, 98 bis Boulevard Arago, 75014 Paris, France
[39] Department of Astronomy, University of Michigan, 1085 S. University Ave., Ann Arbor, MI 48109, USA

ABSTRACT

We present near-infrared spectroscopy of 21 quasars at $6.07 \leq z \leq 6.90$ obtained with JWST/NIRSpec and Subaru/MOIRCS. These targets have absolute ultraviolet magnitudes of $-25 < M_{1450} < -22$ and are drawn from a sample of $z > 6$ quasars identified in the *Subaru High-z Exploration of Low-Luminosity Quasars* (SHELLQs) project. These quasars occupy the intermediate-luminosity regime between luminous quasars and the faint high-redshift AGNs uncovered by JWST. We detect broad Balmer emission lines and Mg II $\lambda 2798$ with underlying continua from the NIRSpec and MOIRCS targets, respectively. The virial black hole masses of this sample span a wide range of $7.2 < \log(M_{\rm BH}/M_\odot) < 9.4$, with Eddington ratios of $-1.3 < \log(L_{\rm bol}/L_{\rm Edd}) < 0.4$. Combining these measurements with our previous mass estimates for other SHELLQs quasars, we construct a sample of 27 quasars with $M_{\rm BH}$ estimates at $6 < z < 7$ and derive the distributions of $M_{\rm BH}$ and $L_{\rm bol}/L_{\rm Edd}$. When compared with luminosity-matched quasars at $z \approx 1.3$, we find median offsets of $\Delta \log(M_{\rm BH}/M_\odot) = -0.4$ and $\Delta \log(L_{\rm bol}/L_{\rm Edd}) = 0.2$ in the high-redshift sample. In addition, 11% of the high-redshift quasars are accreting near or above the Eddington limit. As a systematic check, adopting the Eddington-ratio-dependent calibration of single-epoch $M_{\rm BH}$ estimates increases the inferred super-Eddington fraction to 22%. These results indicate that a representative population of distant supermassive black holes undergo a rapid accretion phase, although not as extreme as that seen in the most luminous quasar population, consistent with the anti-hierarchical growth scenario of supermassive black holes.

Keywords: dark ages, reionization – quasars:general – quasars: supermassive black holes

1. INTRODUCTION

High-redshift ($z > 6$) quasars hold the key to unveiling the early growth pathways of supermassive black holes (SMBHs). Extensive efforts have been made to search for these earliest-formed SMBHs based on $\gtrsim 1,000$ deg^2-scale ground-based wide-field surveys (X. Fan et al. 2023, for a recent review), yielding hundreds of luminous (bolometric luminosity $\log L_{\rm bol}$ [erg s^{-1}] > 47) and massive ($\log M_{\rm BH}$ $[M_\odot] = 8-9$) SMBHs at $6 \leq z \leq 7.8$ (E. Bañados et al. 2018; J. Yang et al. 2020; F. Wang et al. 2021; D. Yang et al. 2026). New-generation infrared surveys are expected to push the redshift frontier even farther. Euclid has begun its full extragalactic sky survey to search for luminous quasars to $z \sim 9$ (Euclid Collaboration et al. 2019; E. Bañados et al. 2025; D. Yang et al. 2026). The Nancy Grace Roman Space Telescope will carry out a deeper infrared survey than Euclid, and will be able to identify relatively faint $z > 7$ quasars over $\sim 2,000$ deg^2 (W. Li et al. 2023; W. L. Tee et al. 2023).

Ultradeep infrared observations by the James Webb Space Telescope (JWST; J. Rigby et al. 2023) have proven effective in identifying low-luminosity active galactic nuclei (AGN), despite the limited field of view of its instruments ($\ll 1$ deg^2). This new population of AGN, with luminosities similar to local Seyfert galaxies at $\log L_{\rm bol}$ [erg s^{-1}] $= 44-45$, appears surprisingly abundant, suggesting that up to a few tens of percent of galaxies host accreting SMBHs at $z > 4$ (e.g., M. Onoue et al. 2023; D. D. Kocevski et al. 2023; Y. Harikane et al. 2023; J. Matthee et al. 2024; J. E. Greene et al. 2024; I. Juodžbalis et al. 2026; A. J. Taylor et al. 2025; H. Umeda et al. 2025). Remarkably, many of these AGN show red optical colors (e.g., J. Matthee et al. 2024), hinting at a scenario in which SMBHs are often surrounded by dense gas (K. Inayoshi & R. Maiolino 2025; A. de Graaff et al. 2026) or dust (F. Vito et al. 2018; Y. Ni et al. 2020; Y. Matsuoka et al. 2025a) at high redshift.

A relatively unexplored parameter space lies between these two populations. This intermediate-luminosity regime ($\log L_{\rm bol}$ [erg s^{-1}] $= 46-47$) holds the key to bridging the well-studied UV-selected luminous quasars and the optically-selected lower-luminosity AGN recently identified by JWST. The 8.2-meter Subaru Telescope has made significant contributions through its wide-field imaging observations with Suprime-Cam (N.

Kashikawa et al. 2015; M. Onoue et al. 2017) and Hyper Suprime-Cam (HSC; S. Miyazaki et al. 2018; H. Aihara et al. 2018). The latter has led to a series of publications from *the Subaru High-z Exploration of Low-Luminosity Quasars* (SHELLQs) project (Y. Matsuoka et al. 2016, 2018a,b, 2019a,b, 2022, 2024, 2025b). These observations are made possible by Subaru's unique capability of wide-field imaging at prime focus. A ten-year survey with Vera C. Rubin Observatory (Ž. Ivezić et al. 2019) will soon explore a similar parameter space in the southern hemisphere (W. L. Tee et al. 2023), albeit over a much larger area.

Spectroscopic follow-up observations are essential to constrain the properties of SMBHs in quasars, as quasar luminosity is determined by the product of SMBH mass and accretion rate. The latter is typically expressed in terms of the Eddington ratio (i.e., $L_{\rm bol}/L_{\rm Edd}$). Beyond distances where direct SMBH mass estimates via stellar kinematics are possible (A. M. Ghez et al. 2008; R. Genzel et al. 2010), single-epoch spectroscopy of broad emission lines from the quasar broad-line region (BLR) is often used to derive virial SMBH masses, while infrared interferometry techniques have recently started to probe BLR kinematics up to $z \sim 4$ (GRAVITY+ Collaboration et al. 2026). The single-epoch method assumes that the BLR gas is gravitationally bound to the central SMBH, such that the broad-line width traces the virial velocity of the BLR gas. The BLR radius ($R_{\rm BLR}$) is inferred from the $R_{\rm BLR}$–continuum luminosity relation calibrated against reverberation mapping (e.g., S. Kaspi et al. 2000; M. Vestergaard 2002; M. C. Bentz et al. 2013).

SMBH mass estimates have been obtained for dozens of luminous $z > 6$ quasars, revealing systematically high Eddington ratios, near or above the Eddington limit (e.g., L. Jiang et al. 2007; C. J. Willott et al. 2010; B. Trakhtenbrot et al. 2017; J. Yang et al. 2021, 2023; E. P. Farina et al. 2022; C. Mazzucchelli et al. 2023; but see Y. Shen et al. 2019). The faint JWST AGNs are more commonly found in the sub-Eddington regime (e.g., J. Matthee et al. 2024; I. Juodžbalis et al. 2026), although the bolometric SEDs of this new population has still been elusive (J. E. Greene et al. 2026). Such observations, however, remain limited in the intermediate-luminosity range (C. J. Willott et al. 2010; Y. Kim et al. 2018; M. Onoue et al. 2019). This is partly due to the high atmospheric infrared sky background in ground-based observations, which effectively limits $M_{\rm BH}$ estimates to quasars brighter than $\approx$ 23 mag in y-band. Among these early studies, M. Onoue et al. (2019, hereafter O19) observed six of the first SHELLQs quasars at near-infrared wavelengths to estimate their SMBH masses from broad Mg II λ2798 emission lines. They showed that the SHELLQs quasars generally accrete at sub-Eddington rates, in contrast to the results of luminous quasars.

A. Takahashi et al. (2024) matched the Lyα profiles of the SHELLQs objects in their discovery spectra with lower-redshift SDSS quasars (I. Pâris et al. 2018), predicting the SMBH mass distribution of the full SHELLQs quasar sample. They found that the masses range from 10^7 to 10^{10} $M_{\rm BH}$. However, direct measurement of broad lines in the rest-frame near-UV and optical is preferable in order to better estimate their SMBH masses. The unprecedented sensitivity of JWST now enables us to directly probe the SMBH masses of the faintest SHELLQs quasars beyond the ground-based limit ($y > 23$ mag), as has been demonstrated in earlier JWST studies of the SHELLQs quasars (X. Ding et al. 2023; M. Onoue et al. 2025; J. Lyu et al. 2025).

In this paper, we present infrared spectroscopy (i.e., rest-frame near-ultraviolet or optical) of an additional 21 SHELLQs quasars at $6.09 \leq z \leq 6.90$ using both JWST and Subaru. Spectroscopic redshifts and SMBH masses of some of these quasars have been published in the literature (R. Ishimoto et al. 2020; J. Wolf et al. 2023; X. Ding et al. 2023; M. Onoue et al. 2025; C. L. Phillips et al. 2026). Specifically, J. D. Silverman et al. (2025) use the SMBH masses of the JWST targets in this paper to constrain the intrinsic distribution of $z = 6$ quasars in the host stellar mass – SMBH mass plane.

This paper is organized as follows: We first present our JWST/NIRSpec observations and spectral analyses in Section 2, and then present our Subaru/MOIRCS observations and their spectral analyses in Section 3. BH mass measurements of these two samples are presented in Section 4. Section 5 gives the summary and our future prospects.

The magnitudes quoted in this paper are in the AB system (J. B. Oke & J. E. Gunn 1983). We correct for instrumental broadening when reporting the emission line widths. We adopt a standard ΛCDM cosmology with $H_0 = 70$ km s^{-1} Mpc^{-1}, $\Omega_m = 0.3$, and $\Omega_\Lambda = 0.7$. Throughout this paper, L_{3000} and L_{5100} denote monochromatic luminosity λL_λ evaluated at rest-frame 3000 Å and 5100 Å, respectively, with $L_{\lambda_{\rm rest}} = 4\pi d_L^2(1+z) f_\lambda[(1+z)\lambda_{\rm rest}]$.

2. JWST/NIRSPEC

We first present the rest-frame optical spectroscopy of our JWST targets.

2.1. *Target Selection*

Our NIRSpec targets were observed as a part of a JWST Cy 1 program (GO 1967; PI: M.Onoue) between

Table 1. Targets & Observations

ID	$z_{\mathrm{Ly}\alpha}$	y_{HSC} [mag]	F150W/K_s [mag]	M_{1450} [mag]	Date	Exp. time [hour]	$\alpha_{\lambda,\mathrm{UV}}$	SNR	Ref.	Notes
JWST/NIRSpec										
J223644.58+003256.9	6.4	23.18 ± 0.05	22.612 ± 0.003	-23.8	2022 Oct. 30	0.6	-0.78 ± 0.10	46	1	*a*
J225538.04+025126.6	6.34	22.94 ± 0.08	22.837 ± 0.003	-23.9	2022 Oct. 28	0.6	-1.78 ± 0.17	32	2	
J114658.89−000537.7	6.30	24.77 ± 0.29	24.775 ± 0.019	-21.5	2023 Jun. 22	2.4	-2.01 ± 0.63	42	2	*b*
J152555.79+430324.0	6.27	23.50 ± 0.09	23.518 ± 0.006	-23.6	2023 Mar. 18	0.9	-2.05 ± 0.20	27	3	
J114648.42+012420.1	6.27	23.12 ± 0.06	22.870 ± 0.003	-23.7	2023 Jun. 22	0.9	-1.47 ± 0.13	39	2	
J084431.60−005254.6	6.25	23.13 ± 0.08	22.553 ± 0.002	-23.7	2022 Nov. 16	0.6	-0.76 ± 0.16	34	4	
J021721.59−020852.6	6.20	23.57 ± 0.08	24.755 ± 0.007	-23.2	2023 Jul. 22	0.9	-2.39 ± 0.17	13	4	*b*
J091833.17+013923.4	6.19	23.19 ± 0.04	23.982 ± 0.004	-23.7	2022 Dec. 25	0.6	-1.57 ± 0.09	29	2	
J084408.61−013216.5	6.18	23.68 ± 0.15	23.976 ± 0.009	-23.7	2022 Nov. 28	0.9	-2.64 ± 0.32	39	2	*b*
J142517.72−001540.8	6.18	23.36 ± 0.06	23.076 ± 0.004	-23.4	2023 Jan. 23	0.6	-1.38 ± 0.12	30	4	
J151248.71+442217.5	6.18	23.27 ± 0.08	23.075 ± 0.004	-23.1	2023 Feb. 14	2.2	-1.59 ± 0.18	75	3	*a, c*
J091114.27+015219.4	6.07	24.33 ± 0.13	23.962 ± 0.009	-22.1	2023 Nov. 28	2.4	-1.20 ± 0.28	23	4	
Subaru/MOIRCS										
J221027.24+030428.5	6.90	22.91 ± 0.06	21.76 ± 0.08	-24.4	2018 Jul. 7, 8	3.1	-0.64 ± 0.12	9.0	2	
J092120.56+000722.9	6.56	21.24 ± 0.01	20.40 ± 0.05	-24.8	2019 Apr. 22	1.2	-1.05 ± 0.06	10.0	2	
J154505.62+423211.6	6.50	22.29 ± 0.04	21.35 ± 0.10	-24.2	2018 Jul. 8, 9 2019 Apr. 22,23	4.5	-1.07 ± 0.12	8.3	2	
J135012.04−002705.2	6.49	22.89 ± 0.05	22.48 ± 0.14	-24.4	2019 Apr. 23	3.7	-1.53 ± 0.17	4.0	3	*d*
J100401.37+023930.9	6.41	22.60 ± 0.03	21.65 ± 0.09	-24.4	2021 Jan. 31	2.8	-0.91 ± 0.11	6.4	2	
J113753.64+004509.7	6.40	22.37 ± 0.03	21.28 ± 0.08	-24.2	2019 Apr. 21, 23	3.7	-0.77 ± 0.10	7.3	3	
J230422.97+004505.4	6.36	22.73 ± 0.05	21.79 ± 0.14	-24.3	2020 Aug. 11	2.3	-0.87 ± 0.18	5.3	2	
J140629.13−011611.1	6.29	21.90 ± 0.03	21.69 ± 0.09	-25.0	2019 Apr. 22	1.9	-1.71 ± 0.12	4.5	2	
J121721.35+013142.5	6.20	20.94 ± 0.01	20.54 ± 0.06	-25.4	2019 Apr. 22	0.9	-1.54 ± 0.07	6.4	5	

NOTE— The targets are grouped by instrument (JWST/NIRSpec at the top and Subaru/MOIRCS at the bottom), and are ordered by decreasing Lyα redshift within each group. The target IDs are based on coordinates, namely Jhhmmss.ss+/−ddmmss.s for a quasar at (R.A., Decl.) = (hh:mm:ss.ss, ±dd:mm:ss.s). We use shorter IDs (Jhhmm±ddmm) elsewhere in the paper. The y-band magnitudes, corrected for Galactic extinction (D. J. Schlegel et al. 1998), are the PSF magnitudes from the Public Data Release 3 of the HSC-SSP catalog (H. Aihara et al. 2022). The NIR photometry is reported, namely the F150W magnitudes for the JWST targets (X. Ding et al. 2025), and Ks-band magnitudes for the MOIRCS targets. The UV continuum slope $\alpha_{\lambda,\mathrm{UV}}$ ($F_\lambda \propto \lambda^{\alpha_\lambda}$) is derived from the y and the NIR band photometry. The signal to noise ratio (SNR) column lists the median continuum SNR calculated over 300 km s^{-1}, which approximately corresponds to the resolution element of the NIRSpec G395M grating. Wavelengths around rest-frame 5100 Å is used for the NIRSpec targets, while the whole spectrum range is used for the MOIRCS targets. The discovery references are as follows: (1) Y. Matsuoka et al. (2016), (2) Y. Matsuoka et al. (2018b), (3) Y. Matsuoka et al. (2019b), (4) Y. Matsuoka et al. (2018a), and (5) E. Bañados et al. (2016) and F. Wang et al. (2017), . Specific spectroscopic properties of the targets are indicated in the Notes column: (*a*) Balmer absorption lines; (*b*) strong narrow emission lines; (*c*) double-peaked Hα; (*d*) a candidate Mg II BAL.

2022 October 28 and 2023 November 28. Ten quasars at $6.18 \leq z \leq 6.4$ and $M_{1450} \geq -24$ mag were selected from a parent sample of $z \sim 6$ quasars that were used to estimate the $z = 6$ quasar luminosity function (Y. Matsuoka et al. 2018c). Two fainter quasars, J1146−0005 and J0911+0152 with $M_{1450} \approx -22$ mag, were added to the sample in order to expand the luminosity range. The basic properties of these 12 quasars are summarized in Table 1. Figure 1 shows the z–M_{1450} distribution of the SHELLQs quasars with available black hole mass estimates, including the JWST/NIRSpec and Subaru/MOIRCS targets presented in this paper, compared with targets of the JWST EIGER (M. Yue et al. 2024) and ASPIRE programs (F. Wang et al. 2023, 2026).

These quasars were also observed with NIRCam with two broadband filters (F150W and F356W). In X. Ding et al. (2023) and X. Ding et al. (2025), we decompose these NIRCam images into a combination of 2D Sérsic profile and point spread function (PSF) for separating host stellar emission from compact quasar emission. One of the targets, J2236+0032, was observed with six additional broad- and medium-band NIRCam filters to constrain their post-starburst stellar population (M. Onoue et al. 2025). In Table 1, we quote the decomposed F150W quasar magnitudes.

2.2. *G395M spectroscopy*

The JWST spectroscopy was performed with the NIRSpec's 0″.2-wide S200A2 fixed slit (P. Jakobsen et al. 2022). We chose the G395M medium-resolution grating, which covers 2.87 – 5.27 μm. This wavelength window corresponds to ≈ 4000–7300 Å in the rest frame of the target quasars. Target acquisition was performed with the wide aperture target acquisition (WATA) method. The on-source exposure times range from 0.6 to 2.4 hours with longer exposures assigned to UV-fainter targets. We achieved these exposures with 3-point primary dithering and no sub-pixel dithers. The NRSIRS2RAPID readout pattern was used for those targets with < 1 hour exposures, while NRSIRS2 for those with HSC y-band magnitude fainter than 24 (J0911+0152, J1146−0005, J1512+4422).

The data reduction of these JWST data follows our earlier publications (X. Ding et al. 2023; M. Onoue et al. 2025). Briefly, the uncal images were downloaded from the MAST archive and processed with the JWST pipeline version 1.17.1 with the parameter reference file jwst_1322.pmap, as registered in the JWST Calibration Reference Data System [40]. Giant cosmic ray hits were masked during the Stage 1 pipeline by turning on the

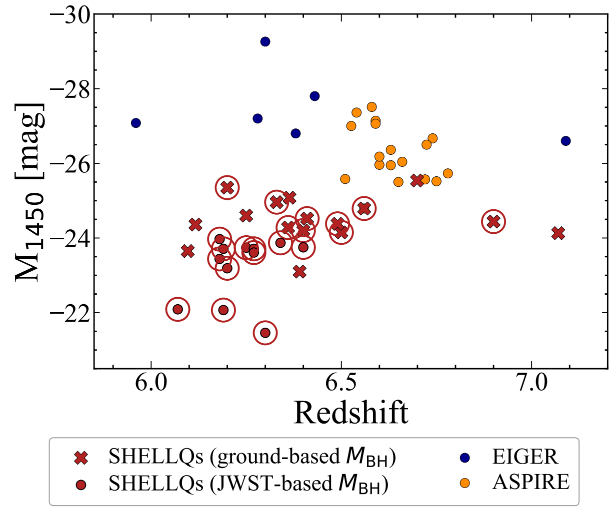

Figure 1. The redshift - M_{1450} distribution of the SHELLQs quasars with available BH mass estimates (red). Those with Balmer-line-based $M_{\rm BH}$ estimates available from JWST observations are shown as small circles, and those with Mg II-based $M_{\rm BH}$ estimates from ground-based observations are shown as crosses. The SHELLQs quasars presented in this paper are highlighted with outer circles. The remaining SHELLQs quasars, all with Mg II-based $M_{\rm BH}$ estimates, are taken from O19, Y. Matsuoka et al. (2019a), and N. Kato et al. (2020). Luminous quasars targeted in the JWST EIGER program (blue; M. Yue et al. 2024) and the ASPIRE program (orange; F. Wang et al. 2023, 2026) are also shown for comparison.

expalnd_large_events and sat_required_snowball functions implemented in the "jump" step. Smaller cosmic rays near the target traces were also flagged with visual inspection. The $1/f$ noise stripes were subtracted before the Stage 2 pipeline based on a public code implemented in *msaexp* (G. Brammer 2023). The point-source pathloss correction was applied during the Stage 2 pipeline reduction to take into account slit losses. The processed two-dimensional spectra at each dither position were stacked using the Stage 3 pipeline with inverse-variance weighting. One-dimensional spectra were extracted with a 6-pixel-wide (0″.6 wide) box-car aperture. Figure 2 shows the full spectra of the JWST targets. The median signal to noise ratios per pixel at rest-frame 5100 ± 50 Å range from 10 – 50 (Table 1).

We note that C. L. Phillips et al. (2026) use the Stage 2 spectra of the same data to model the 2D PSF and subtract the quasar component from each dither. This approach was taken to avoid the artificial broadening of the PSF that occurs during Stage 3 resampling and rectification, thereby ensuring the accurate extraction of extended host stellar and gas emission.

[40] https://jwst-crds.stsci.edu

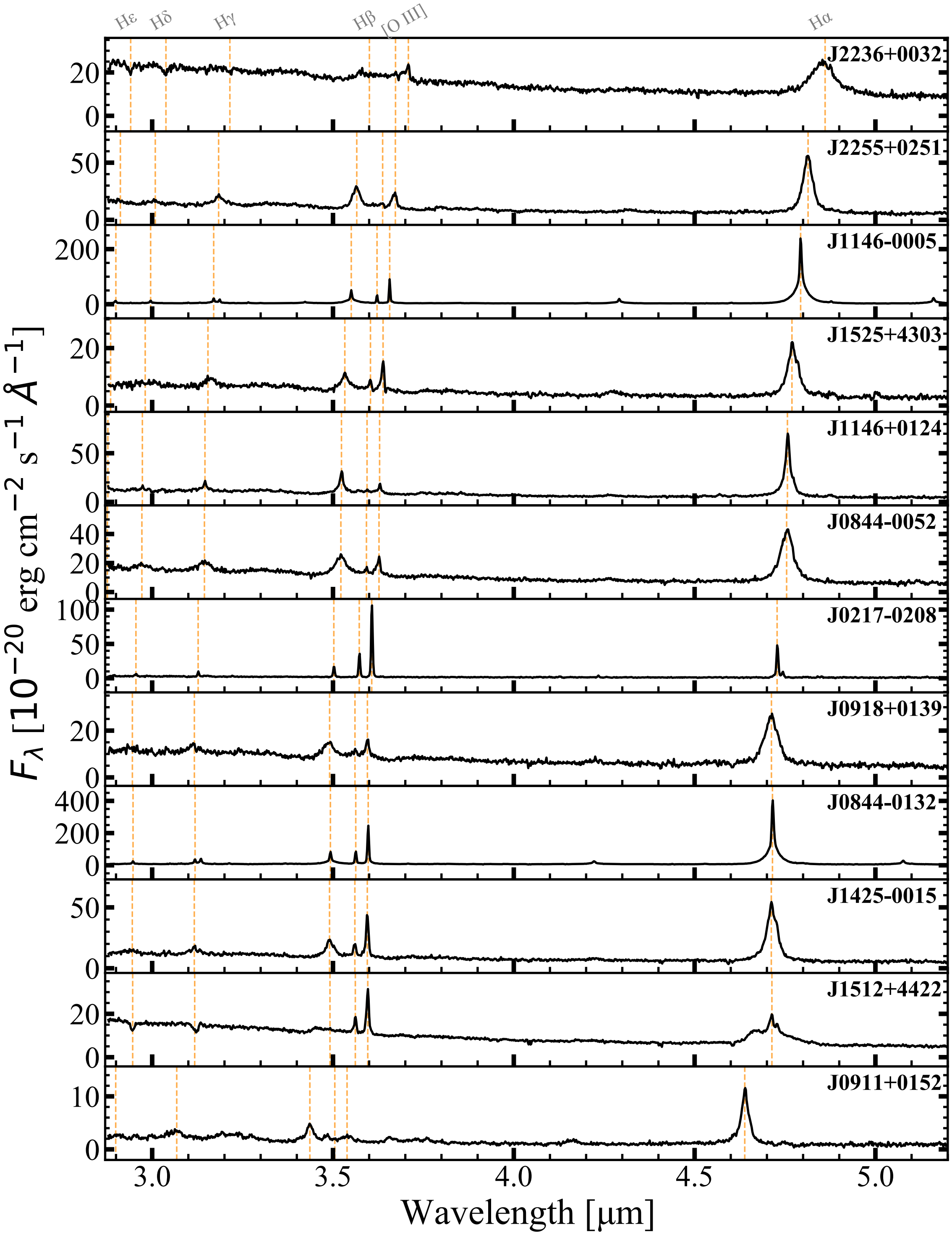

Figure 2. The NIRSpec G395M spectra of the JWST targets. Flux densities are presented in units of 10^{-20} erg cm^{-2} s^{-1} Å^{-1}. The observed wavelengths of Balmer lines and [O III] are indicated by vertical orange dashed lines. For J2236+0032 and J1512+4422, Hγ, Hδ, and Hϵ are seen in absorption. Weaker emission lines are also identified in the data, such as [O III] λ4364 for some objects.

2.3. *Spectral Fitting*

We model the rest-frame optical spectra of the 12 JWST targets using QSOFitMORE (Y. Fu 2021, version 1.2.0) with custom modifications to fit the continuum and emission lines simultaneously. This is a wrapper package of PyQSOFit (H. Guo et al. 2018; Y. Shen et al. 2019), a public tool widely applied to large spectroscopic datasets such as SDSS (Q. Wu & Y. Shen 2022). A single power-law function is adopted to model the quasar continuum, namely $F_\lambda \propto \lambda^{\alpha_\lambda}$, where α_λ is the slope index. In QSOFitMORE, the pseudo-continuum of ionized iron is taken into account based on a spectrum of a local AGN by T. A. Boroson & R. F. Green (1992). For J2236+0032 and J1512+4422, which show Balmer absorption lines, we perform spectroscopic decomposition to separate the host stellar emission lines from the quasars, and derive the quasar continuum model. A full description of the analysis is presented in M. Onoue et al. (2025). For J0217−0208 and J0844−0132, which show weak continuum and strong narrow emission lines, we model the continuum shape by taking the median flux density every 5000 km s^{-1} in velocity space, with strong emission line regions masked, and interpolate with a third-order spline curve. This smoothed continuum model is subtracted before fitting emission lines. J1146−0005 is as faint as J0217−0208 and J0844−0132 in continuum, but a single power-law model returns a satisfactory fit.

A two-step approach was adopted to model the spectra. First, we run QSOFitMORE to fit the Hβ+[O III] spectral complex in addition to the continuum and iron emission, modeling each line with one or more Gaussian profiles. For Hβ, we adopt a combination of broad and narrow components, where we limit the line width of broad lines to $1,200 \leq \mathrm{FWHM} < 10,000$ km s^{-1}, following Y. Shen et al. (2011), and the widths of narrow lines to FWHM $< 1,200$ km s^{-1}. In most cases, a single broad component is sufficient to fit the broad components. If multiple broad components are required, we use the total FWHM of the composite fit as their line widths. The forbidden [O III] $\lambda\lambda4960, 5008$ lines are modeled with one narrow and one broader component for each of the doublet lines. The latter component is often blueshifted, commonly interpreted as a signature of outflowing ionized gas kinematics. The narrow component of the two [O III] lines are required to have the same line widths without velocity offsets. The line width of the broad [O III] component is left unconstrained and is allowed to have a velocity offset of $|\Delta v| \leq 5,000$ km s^{-1} from the systemic redshifts. We repeat the Hβ+[O III] fitting a few times, updating the redshift at each iteration based on the peak wavelength of the narrow [O III] component. The initial redshift is set to the Lyα redshift, and the final converged [O III] redshift is adopted as the systemic redshift of each quasar. We note that the [O III] emission lines of J0911+0152 are weak, making it difficult to decompose them into two components, and thus their line flux measurements may be degenerate.

We then extend the line fitting to all emission lines visually identified in each spectrum. Forbidden lines, such as [N II] $\lambda\lambda6549, 6585$ and [S II] $\lambda\lambda6718, 6732$, are constrained to have the same line width as the narrow [O III] component. Permitted lines, including the Balmer and Helium lines, are fitted with a combination of one broad and one narrow Gaussian profile, as was done for Hβ. The broad components of individual Balmer lines are fitted independently. In some cases, two or three broad Gaussian profiles are required to fit broad Balmer lines, similar to Hβ. The line widths for the broad components are measured independently for different emission lines, including different Balmer transitions (Section 2.5.2). The narrow components of these permitted lines are fitted using the same FWHM as the narrow [O III] component. This reflects the assumption that the narrow-line region gas shares the same kinematics regardless of the line species. We include [N II] only when the line peak of [N II] $\lambda6585$ is clearly visible in the spectra. The final continuum and emission line models are presented in Figure 3. Table 2 presents the continuum luminosity and line luminosities of representative emission lines. Some of the diagnostic emission line ratios (i.e., [O III]/Hβ and [N II]/Hα) are also presented in C. L. Phillips et al. (2026).

2.4. *Notes on Individual Objects*

Here we describe several remarkable properties of the JWST targets in detail.

J2236+0032: J2236+0032 is one of the two quasars in the sample, in which the spectrum of the host galaxy is immediately apparent. Its high-order Balmer lines (Hγ, Hδ, Hϵ) are observed as absorption lines, unlike those of typical broad-line quasars. We interpret these Balmer absorption lines as the spectroscopic signature of the post-starburst stellar population of the host (M. Onoue et al. 2025). We also highlight that J2236+0032 and J1512+4422 (see below) are hosted by the two most massive galaxies in our sample (X. Ding et al. 2023, 2025). This is consistent with the picture that quasar-mode feedback becomes important as massive galaxies mature and transition toward quiescence, as described in M. Onoue et al. (2025).

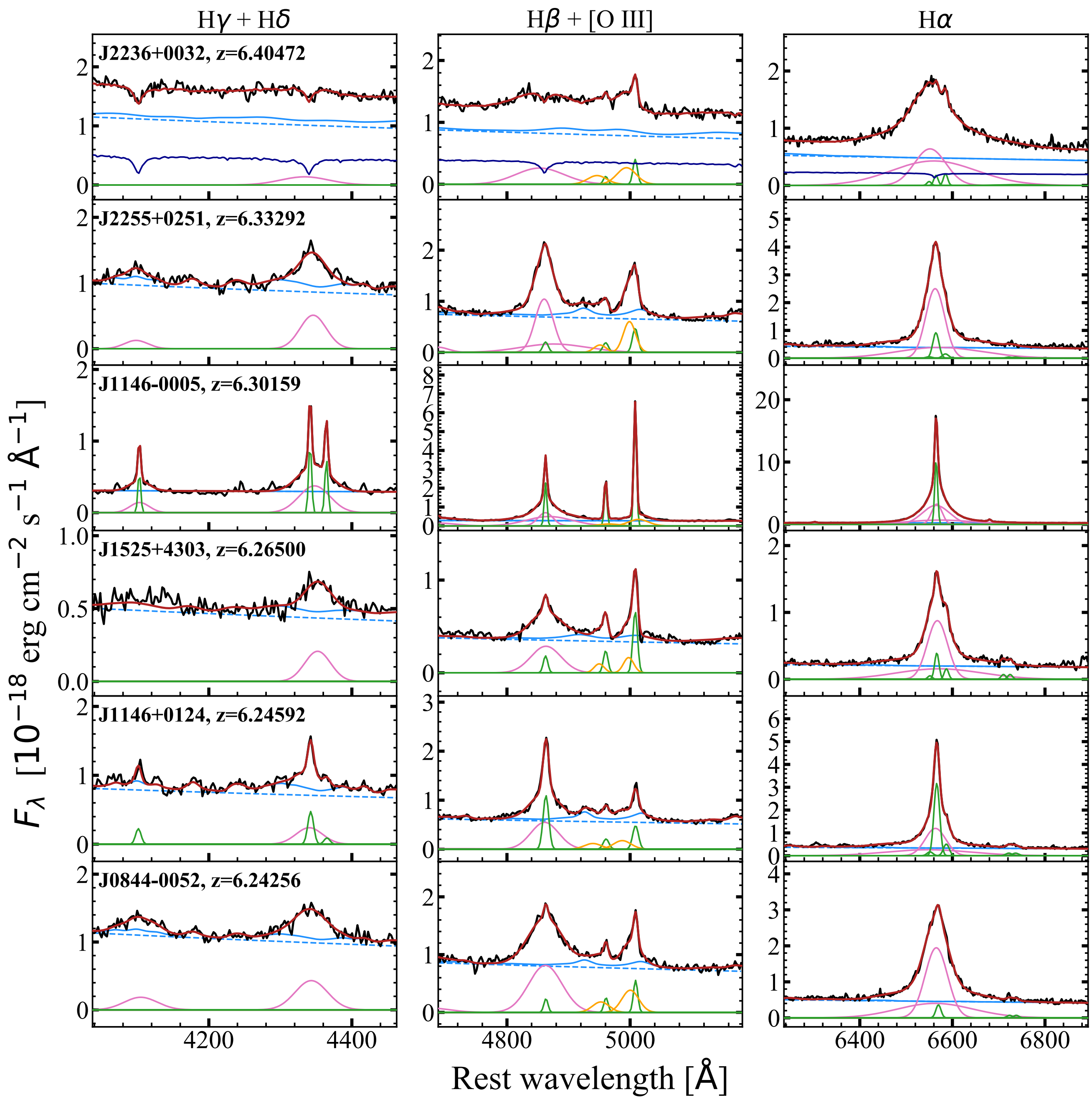

Figure 3. Spectral models for the first half of the JWST targets in the rest frame. Note the different y-axis scale from Figure 2. For each target, the Hγ+Hδ, Hβ+[O III], and Hα spectral regions are shown in the left, middle, and right panels, respectively. The continuum-only and continuum+iron models are shown as blue dashed and blue solid lines, respectively. The host-galaxy stellar continuum for J2236+0032 taken from M. Onoue et al. (2025), is shown as a dark blue line. Emission line models are presented individually with broad components shown as magenta lines and narrow components as green lines. The blueshifted [O III] "wing" components are shown as an orange line. The sum of all line components is shown as a red line.

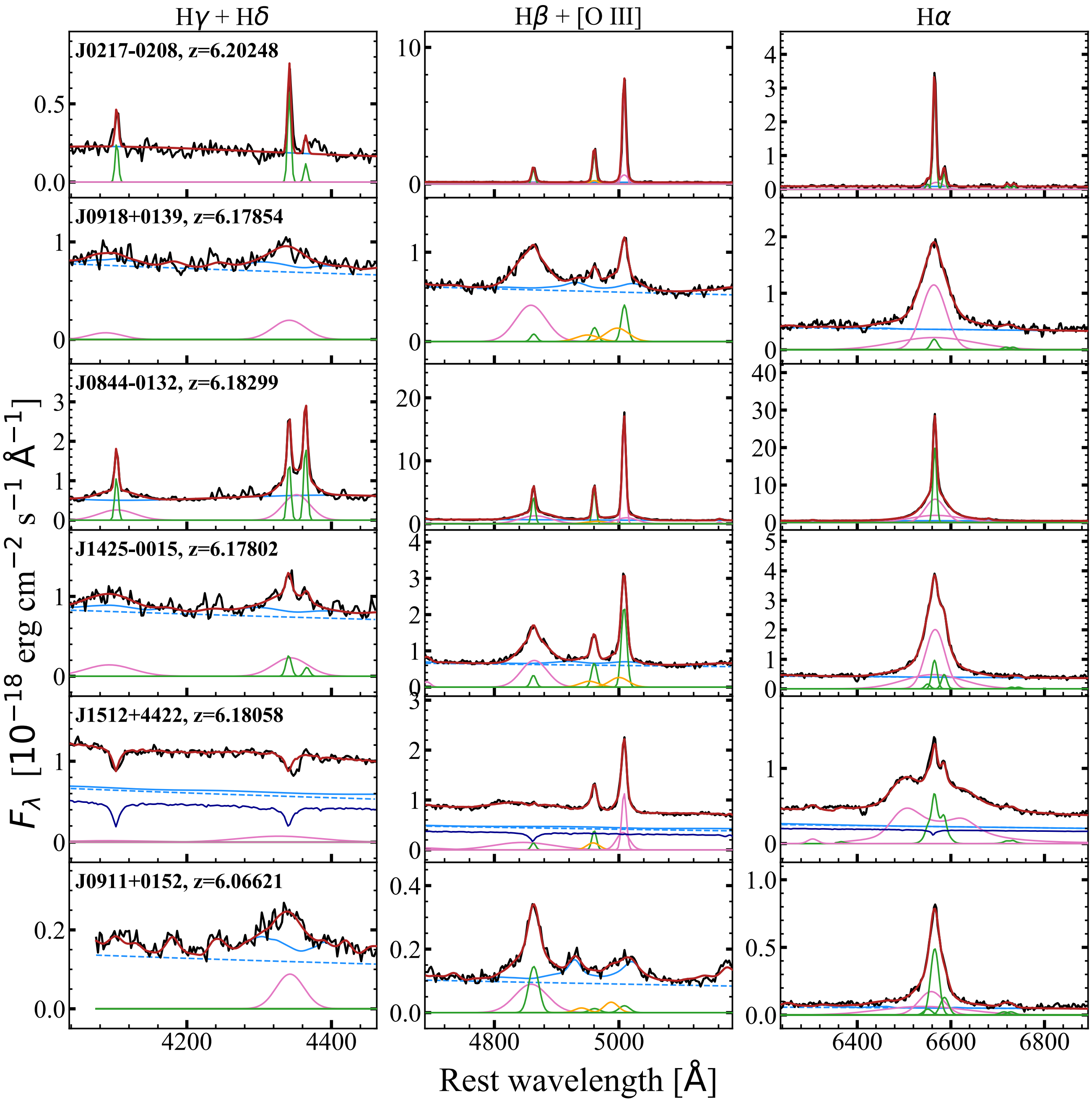

Figure 4. Figure 3, but for the second half of the JWST targets. 1512+4422 shows Balmer absorption lines, similar to J2236+0032, and also exhibits a double-peaked Hα profile (M. Onoue et al. 2025). Zoom-in panels of the Balmer emission lines of J0217−0208 are presented in Figure 10.

Table 2. Spectral properties: JWST targets

ID	$z_{[OIII]}$	L_{5100}	$L_{5100,QSO}$	α_{opt}	FWHM Hβ_b	FWHM Hα_b	FWHM [O III], c	$L_{H\beta,b}$	$L_{H\beta,n}$	$L_{H\alpha,b}$	$L_{H\alpha,n}$
		[10^{45} erg s^{-1}]	[10^{45} erg s^{-1}]		[km s^{-1}]	[km s^{-1}]	[km s^{-1}]	[10^{43} erg s^{-1}]	[10^{43} erg s^{-1}]	[10^{43} erg s^{-1}]	[10^{43} erg s^{-1}]
J2236+0032	6.40472 ± 0.00087	2.550 ± 0.010	1.780 ± 0.012	−1.79 ± 0.02	5644 ± 741	4999 ± 88	412 ± 61	1.18 ± 0.14	···	7.09 ± 0.10	0.09 ± 0.01
J2255+0251	6.33292 ± 0.00096	1.450 ± 0.010	1.310 ± 0.009	−1.96 ± 0.02	2338 ± 44	2405 ± 36	552 ± 51	2.73 ± 0.06	0.10 ± 0.02	9.81 ± 0.12	0.69 ± 0.06
J1146-0005	6.30159 ± 0.00001	0.612 ± 0.001	0.612 ± 0.001	−0.58 ± 0.01	2501 ± 67	1945 ± 349	···	3.00 ± 0.01	0.56 ± 0.01	19.60 ± 1.46	3.61 ± 0.39
J1525+4303	6.26500 ± 0.00054	0.720 ± 0.006	0.582 ± 0.005	−1.91 ± 0.02	3534 ± 81	2620 ± 33	420 ± 28	0.77 ± 0.02	0.07 ± 0.01	3.71 ± 0.05	0.21 ± 0.02
J1146+0124	6.24591 ± 0.00045	1.180 ± 0.005	0.976 ± 0.004	−1.81 ± 0.03	3240 ± 97	2719 ± 110	590 ± 14	1.35 ± 0.01	0.55 ± 0.02	5.55 ± 0.21	2.15 ± 0.14
J0844-0052	6.24256 ± 0.00047	1.630 ± 0.013	1.560 ± 0.012	−1.87 ± 0.02	3913 ± 162	2943 ± 56	377 ± 66	2.41 ± 0.11	0.09 ± 0.01	8.78 ± 0.09	0.22 ± 0.04
J0217-0208	6.20248 ± 0.00001	0.278 ± 0.001	0.0858 ± 0.0004	−2.18 ± 0.04	1154 ± 1	1806 ± 119	230 ± 2	0.09 ± 0.01	0.31 ± 0.01	0.22 ± 0.01	1.23 ± 0.02
J0918+0139	6.17854 ± 0.00139	1.160 ± 0.007	1.080 ± 0.006	−1.58 ± 0.02	3548 ± 121	3149 ± 39	643 ± 54	1.07 ± 0.03	0.04 ± 0.01	5.19 ± 0.03	0.14 ± 0.02
J0844-0132	6.18299 ± 0.00001	1.170 ± 0.003	1.130 ± 0.003	−0.45 ± 0.02	3633 ± 43	2650 ± 17	259 ± 1	3.39 ± 0.01	1.30 ± 0.01	25.60 ± 0.06	8.23 ± 0.02
J1425-0015	6.17801 ± 0.00047	1.250 ± 0.010	1.030 ± 0.008	−1.53 ± 0.03	3038 ± 51	2547 ± 32	537 ± 20	1.65 ± 0.03	0.15 ± 0.02	7.72 ± 0.06	0.59 ± 0.02
J1512+4422	6.18058 ± 0.00063	1.520 ± 0.005	0.934 ± 0.004	−2.20 ± 0.01	4620 ± 97	8590 ± 181	440 ± 25	0.85 ± 0.02	0.055 ± 0.004	4.21 ± 0.03	0.51 ± 0.01
J0911+0152	6.06621 ± 0.00028	0.180 ± 0.002	0.162 ± 0.001	−2.02 ± 0.04	3770 ± 583	3475 ± 70	1147 ± 411	0.24 ± 0.03	0.12 ± 0.05	1.06 ± 0.02	0.45 ± 0.02

NOTE— The continuum slopes α_{opt} are based on observed NIRSpec continuum without subtracting host contribution. The errorbars reported here do not include flux calibration uncertainties.

J1512+4422: J1512+4422 is the other quasar in our sample that shows Balmer absorption lines in Hγ and Hδ. We also observed double-peaked broad Hα emission, in addition to narrow Hα+[N II] and [S II]. M. Onoue et al. (2025) model this line multiplet with a disk BLR model, where the emission arises from relativistic Keplerian motion of gas in the BH accretion disk (M. Eracleous et al. 2009; C. Ward et al. 2024). W. Liu et al. (2026) recently obtained a high-resolution spectrum of this object, where they resolve the Balmer absorption lines and detected a spatially extended ionized gas outflow.

J0844−0132 & J1146−0005: These two quasars are characterized by strong narrow emission lines in the Balmer series on top of their broad components. We detect several other weak emission lines, especially [O III] λ4362, [O I] λ6302, and various transitions of He I. They are distinguished from the other JWST targets by both their continuum slopes and their large Hα/Hβ flux ratios, and rather reminiscent of "Little Red Dot" objects (see Sec 2.5).

J0217−0208: This quasar shows the narrowest Lyα line among our targets and is classified as a narrow-line quasar in the series of the SHELLQs papers (Y. Matsuoka et al. 2018b). The JWST medium-resolution spectrum of J0217−0208 shows that its optical lines are also relatively narrow (FWHM (H$\alpha_{\rm broad} = 1,810 \pm 120$ km s^{-1}). Its line modeling and nature (an AGN or a star-forming galaxy) will be extensively discussed in Section 2.7.

2.5. *Spectral Properties*

2.5.1. *Continuum*

The clear detection of rest-frame optical continuum emission of the NIRSpec targets enables us to investigate their continuum shapes. Figure 5 compares UV and optical slopes of the NIRSpec targets, where the optical slopes $\alpha_{\lambda,\rm optical}$ are derived from the NIRSpec data. The UV continuum slopes $\alpha_{\lambda,\rm UV}$ are obtained from HSC y-band photometry and F150W photometry of the targets (X. Ding et al. 2025). We note that total continuum emission and photometry are used here in order to obtain the observed continuum shape of each object, and part of the measured flux may be contributed by host-galaxy emission.

Figure 5 shows that the NIRSpec targets generally have blue UV continuum shapes, consistent with typical unobscured quasars at $1 < z < 2$ (e.g., $\alpha_{\lambda,\rm UV} \approx -1.7$; D. E. Vanden Berk et al. 2001; J. Selsing et al. 2016). Most targets also show blue optical slopes with $\alpha_{\lambda,\rm optical} < -1.5$, again comparable to those of low-redshift quasars. These similarities in the UV and optical continuum slopes suggest that the accretion-disk emission in the majority of these $z > 6$ quasars is similar to that in lower-redshift quasars.

On the other hand, there are two objects, J0844−0132 and J1146−0005, which stand out with relatively redder optical slopes with $\alpha_{\lambda,\rm optical} \approx -0.5$. The SED of these objects lie between those of normal quasars and Little Red Dot (LRD) objects, which exhibit "V-shape" continuum shapes (J. Matthee et al. 2024; J. E. Greene et al. 2024; D. D. Kocevski et al. 2025). A plausible explanation of the characteristic continuum emission of LRDs is that their optical continuum is thermal emission from a dense gas cocoon surrounding a young black hole (K. Inayoshi & R. Maiolino 2025; A. de Graaff et al. 2025; R. P. Naidu et al. 2025). In this context, J0844−0132 and J1146−0005 may trace an intermediate phase in the evolutionary sequence from LRD-like young accreting black holes to more mature unobscured quasars.

The location of J0844−0132 and J1146−0005 in Figure 5 is also similar to a sub-sample of the SHELLQs quasars, for which their Lyα emission is narrow (FWHM < 500 km s^{-1}) and strong (line luminosity $L_{\rm Ly\alpha} > 10^{44}$ erg s^{-1}). Y. Matsuoka et al. (2025a) show that seven out of ten targets exhibit broad Balmer emission lines in their JWST/NIRSpec observations, indicating that they are modestly dust-obscured quasars. J1146−0005 is among the same population (FWHM $= 330 \pm 100$ km s^{-1}), while J0844−0132 shows a broader Lyα (FWHM $= 1610 \pm 280$ km s^{-1}). This similarity in continuum shapes therefore suggests that J0844−0132 and J1146−0005 represent a related population to the Y. Matsuoka et al. (2025a)'s obscured quasar sample bridging LRDs and normal quasars.

2.5.2. *Balmer Line Widths*

Lower-redshift quasar studies have shown that the broad components of high-order Balmer emission lines exhibit systematically broader profiles than Hα (J. E. Greene & L. C. Ho 2005; A. Schulze & L. Wisotzki 2010; A. Schulze et al. 2018). These lines also show shorter response times to continuum flux variations in reverberation mapping (M. C. Bentz et al. 2010; C. J. Grier et al. 2017), suggesting that higher-order Balmer lines originate from inner regions of the BLR gas.

In Figure 6, we show the relation between line FWHMs of different Balmer series transitions in our sample. We perform orthogonal distance regression (ODR) in logarithmic space to fit a linear relation for each line combination (Hα vs Hβ, Hγ, and Hδ), namely

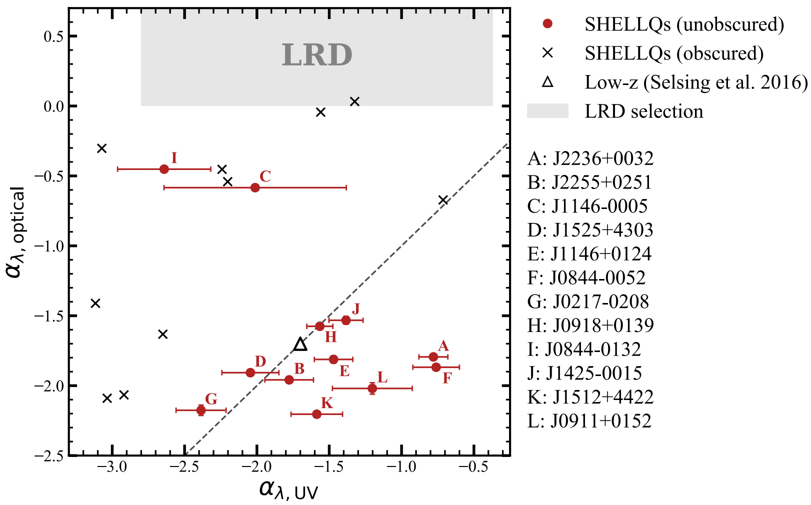

Figure 5. UV ($\alpha_{\lambda,\rm UV}$) and optical ($\alpha_{\lambda,\rm optical}$) continuum slopes. The JWST targets in this work are shown as red circles with each object labeled by a letter as indicated in the lower right. The dust-obscured broad-line SHELLQs objects observed by Y. Matsuoka et al. (2025a) are shown as black crosses. The continuum slopes of typical $1 < z < 2$ quasars measured by J. Selsing et al. (2016) are shown as an open triangle. The color window used for the selection of Little Red Dots in D. D. Kocevski et al. (2025) is indicated by the shaded region. The dashed line indicates the 1:1 relation.

Table 3. Correlations of Balmer emission line widths

Line	Intercept †	$\rm FWHM_{H\alpha}/FWHM_{line}$
Hβ	-0.066 ± 0.027	0.86 ± 0.05
Hγ	-0.087 ± 0.018	0.82 ± 0.03
Hδ	-0.18 ± 0.03	0.66 ± 0.04

NOTE—† The intercept a in the relation $\log_{10} \rm FWHM_{H\alpha} = \log_{10} FWHM_{line} + \mathit{a}$ is obtained using ODR regression. The intercept for each line combination is also presented in the form of $\rm FWHM_{H\alpha}/FWHM_{line}$ ($= 10^a$) in the third column.

$\log_{10} \rm FWHM_{H\alpha} = \log_{10} FWHM_{line} + \mathit{a}$, where a is the intercept. We chose ODR to take into account measurement errors in both variables. We here only consider broad components of the Balmer emission lines and remove J1512+4422, which exhibits a double-peak profile in Hα (M. Onoue et al. 2025). We impose a 5% error floor on the measurement errors to prevent the fitting from being dominated by specific objects with small errors. The slope of each relation is fixed to 1, given the limited dynamic range and the small sample size.

The best-fit parameters of the fits are reported in Table 3. We find that the line widths of high-order transitions are generally broader than Hα. The majority are consistent with the relation of lower-redshift quasars (J. E. Greene & L. C. Ho 2005; A. Schulze et al. 2018) with Hβ broader than Hα by 16%. For higher-order transitions, the linear regression finds that Hγ and Hδ are 22% and 51% broader than Hα, respectively. Our results therefore indicate that the low-redshift trends among different Balmer transitions extend to $z \sim 6$.

On the other hand, J0217−0208 and J0911+0152 are outliers with FWHM(Hα) > FWHM(Hβ), which would bring the mean relation closer to the one-to-one relation. A larger sample would therefore be required to firmly establish the high-redshift line width relation. Also note that the weak Hδ emission line is sensitive to continuum and iron emission uncertainties.

2.5.3. *Continuum – Balmer Line Relation*

Local AGN show a tight correlation between the AGN continuum and Balmer line luminosities (J. E. Greene & L. C. Ho 2005; G. La Mura et al. 2007). This relation enables single-epoch BH mass estimates solely from Balmer emission lines without needing to determine the AGN continuum, which may be affected by possible contribution of host stellar emission. Using our JWST sample, we now investigate whether the local continuum–Balmer luminosity relation holds for high-redshift quasars.

The rest-frame 5100 Å continuum luminosity L_{5100} is measured from the best-fit continuum model to the observed NIRSpec spectra. We then subtract the host stellar emission by leveraging our NIRCam imaging data analysis presented in X. Ding et al. (2023) and X. Ding et al. (2025). Specifically, we refer to the fraction of stellar emission in the NIRCam F356W images of the JWST

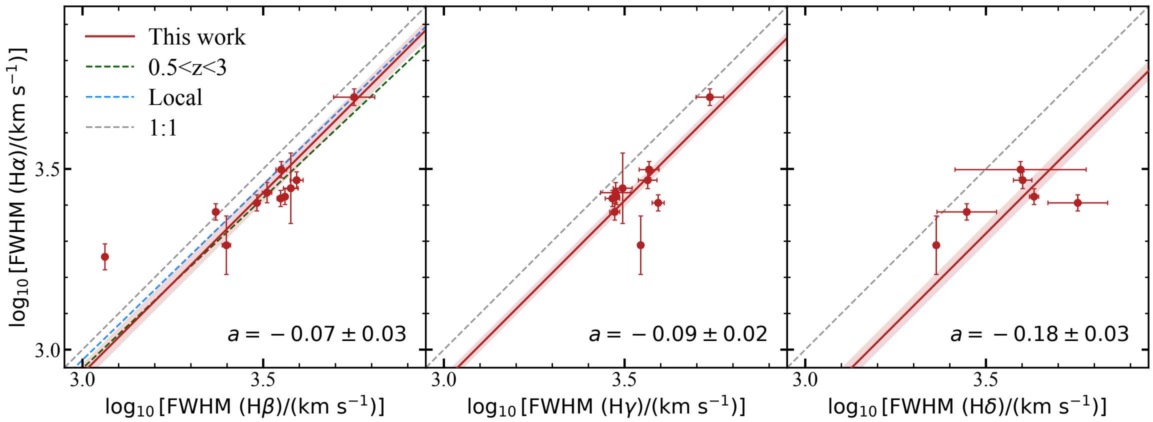

Figure 6. Comparison of the FWHMs of broad Balmer emission lines. Red solid lines show the line correlation where the slope is fixed to 1. Grey dashed lines show the one-to-one relation. In the Hα vs Hβ plot, the local relation of J. E. Greene & L. C. Ho (2005) and the relation at $0.5 < z < 3$ from A. Schulze et al. (2018) are indicated by cyan and green dashed lines, respectively.

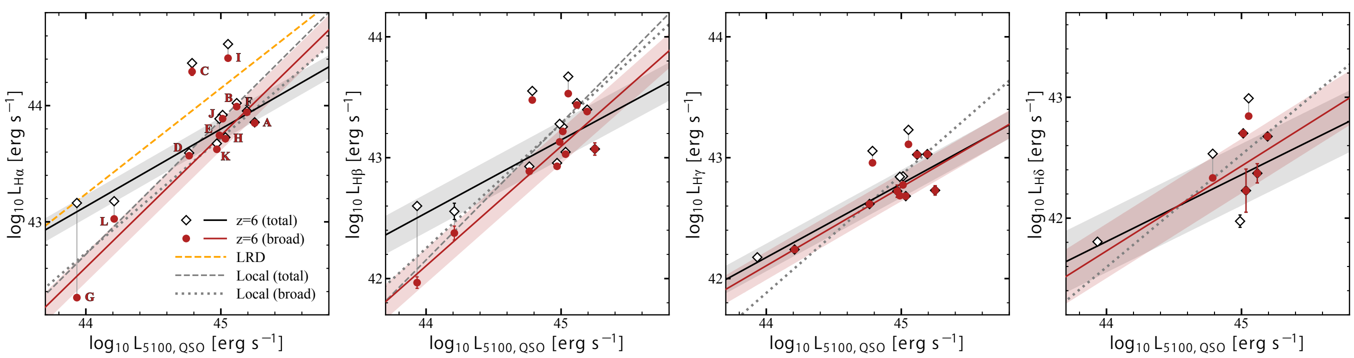

Figure 7. Correlations between 5100 Å luminosity and Balmer line luminosities from Hα to Hδ. Here we use the host–galaxy–subtracted 5100 Å luminosity ($L_{5100,\mathrm{QSO}}$) based on JWST/NIRCam F356W imaging decomposition (X. Ding et al. 2025). In each panel, the luminosities of the broad-line components are shown as red circles, while those including both broad and narrow components are shown as open black diamonds. For each line pair, the best-fit linear relation is plotted as a solid line with the shaded area indicating the 1σ scatter of the residuals relative to the best-fit relation. The gray dashed and dotted lines represent the correlations observed in the local universe for the total (J. E. Greene & L. C. Ho 2005) and broad-only (G. La Mura et al. 2007) luminosities, respectively. For the $L_{5100,\mathrm{QSO}}$-$L_{\mathrm{H}\alpha}$ panel, the relation for $z < 4.5$ LRDs from A. de Graaff et al. (2026) is shown with an orange dashed line. The two outliers in our sample (J0844−0132 and J1146−0005) fall at the upper left in all panels.

targets, which trace rest-frame $4,300$–$5,500$ Å at the redshifts of our targets, and derive the host-subtracted 5,100 Å continuum luminosity $L_{5100,\mathrm{QSO}}$. For the two post-starburst quasars, J2236+0032 and J1512+4422, we use the spectroscopically-decomposed quasar spectra presented in M. Onoue et al. (2025) to evaluate the quasar-only continuum luminosity.

We fit the quasar continuum–Balmer luminosity relations to the following form:

$$\log(L_{\mathrm{Balmer}}\,[\mathrm{erg\ s^{-1}}]/10^{42}) = a\log(L_{5100,\mathrm{QSO}}\,[\mathrm{erg\ s^{-1}}]/10^{44}) + b, \quad (1)$$

where a and b represent the slope and intercept, respectively. We exclude J0844−0132 and J1146−0005 from this fitting, as their LRD-like continuum shapes and high Hα/Hβ ratios indicate that they are a distinct population from the other objects studied here (Sections 2.5.1, 2.5.4). We note that these two objects lie far from the regression of the other objects in the continuum – Balmer emission line luminosity plane. The fitting results are summarized in Table 4.

Figure 7 shows the best-fit correlations between $L_{5100,\mathrm{QSO}}$ and L_{Balmer}. For comparison, Figure 7 also shows the local total-line relation of J. E. Greene & L. C. Ho (2005) and the broad-line-only relation of G. La Mura et al. (2007). In the Hα panel, we also show the correlation for $z < 4.5$ LRDs obtained in A. de Graaff et al. (2026); their sample is fainter than ours in the quasar continuum ($L_{5100} < 10^{44}$ erg s^{-1}). We find that the best-fit relation between quasar op-

Table 4. Correlations between $L_{5100,\rm QSO}$ and $L_{\rm Balmer}$

Relation	a	$10^{\,a}$	b	σ
$\rm H\alpha_{broad}$	0.69 ± 0.08	4.89 ± 0.90	1.05 ± 0.08	0.10
$\rm H\alpha_{total}$	1.14 ± 0.08	13.8 ± 2.6	0.66 ± 0.09	0.11
$\rm H\beta_{broad}$	0.13 ± 0.12	1.35 ± 0.37	0.96 ± 0.12	0.15
$\rm H\beta_{total}$	0.54 ± 0.13	3.47 ± 1.01	0.60 ± 0.13	0.17
$\rm H\gamma_{broad}$	0.21 ± 0.15	1.63 ± 0.57	0.53 ± 0.15	0.13
$\rm H\gamma_{total}$	0.21 ± 0.09	1.62 ± 0.34	0.58 ± 0.10	0.12
$\rm H\delta_{broad}$	-0.20 ± 2.08	0.63 ± 3.01	0.63 ± 1.90	0.22
$\rm H\delta_{total}$	-0.21 ± 0.27	0.62 ± 0.38	0.56 ± 0.27	0.26
$\rm H\beta$ – $\rm H\alpha$ (broad)	0.64 ± 0.03	4.35 ± 0.26	1 (fixed)	0.08
$\rm H\beta$ – $\rm H\alpha$ (total)	0.64 ± 0.02	4.41 ± 0.23	1 (fixed)	0.07

The results of linear least-χ^2 fits after excluding the two objects exhibiting strong narrow Balmer emission (J0844−0132 and J1146−0005; see text) are presented in this table. For the continuum–Balmer line relations, the fitting form is $\log(L_{\rm Balmer}\ [\rm erg\ s^{-1}]/10^{42}) = a\log(L_{5100,\rm QSO}\ [\rm erg\ s^{-1}]/10^{44}) + b$, where $L_{5100,\rm QSO}$ is the QSO-only continuum luminosity derived from our NIRCam image decomposition analysis presented in X. Ding et al. (2025). The first column lists the Balmer line used as $L_{\rm Balmer}$. We show the correlation for both broad and total Balmer emission lines. We also introduce σ, which represents the intrinsic scatter. For the Hα–Hβ relation, the slope is fixed to unity, namely $\log_{10} L_{\rm H\alpha} = a + \log_{10} L_{\rm H\beta}$.

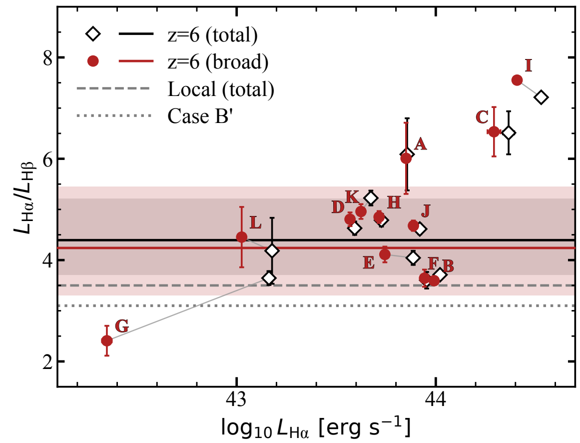

Figure 8. Balmer decrements, $L_{\rm H\alpha}/L_{\rm H\beta}$, as a function of the Hα luminosity. The symbols are the same as in Figure 7, and the gray lines connect the total and broad-component measurements for the same object. The solid black and red lines represent the linear regression for the total and broad emission-line luminosities, respectively, with the shaded regions indicating their uncertainties. The dashed line represents the local relation for the total luminosities (J. E. Greene & L. C. Ho 2005), while the gray dotted line indicates the fiducial Case B′ ratio for AGN NLR gas ($L_{\rm H\alpha}/L_{\rm H\beta} = 3.1$; J. P. Halpern & J. E. Steiner 1983; D. E. Osterbrock & G. J. Ferland 2006).

tical continuum and Hα, effectively equivalent to Hα equivalent widths, is similar to the local relations. At $L_{5100,\rm QSO} = 10^{45}$ erg s^{-1}, the $z = 6$ relation is slightly lower than the J. E. Greene & L. C. Ho (2005) relation by 0.08 dex in Hα total luminosity, and is still consistent within the object-to-object scatter (0.10 dex). The luminosity of broad Hα is well aligned with the G. La Mura et al. (2007) relation at the same luminosity range.

For Hβ and the higher-order Balmer transitions, we also do not find substantial differences between the local relations and those measured for our $z = 6$ sample. For Hβ, the $z = 6$ relations are offset by −0.14 dex for the total luminosity and −0.19 dex for the broad-component luminosity at $L_{5100,\rm QSO} = 10^{45}$ erg s^{-1}. These modest offsets have little impact on single-epoch black hole mass estimates because the inferred mass depends only weakly on the continuum luminosity, scaling as $M_{\rm BH} \propto L_{5100}^{0.5}$, and therefore changes $M_{\rm BH}$ by less than 0.1 dex. This is well below the typical systematic uncertainty of $\sim$ 0.4 dex associated with single-epoch virial mass estimates (M. Vestergaard & B. M. Peterson 2006; Y. Shen 2013). We emphasize that a larger sample with a wider luminosity coverage would be required to firmly establish the high-redshift continuum – Balmer emission line relation.

2.5.4. *Balmer Decrement*

We show in Figure 8 the luminosity ratios of Hα and Hβ of the JWST targets as a function of Hα luminosity. We perform linear regression for both broad-line luminosity and total line luminosity, namely

$$\log_{10} L_{\rm H\alpha} = a + \log_{10} L_{\rm H\beta}, \tag{2}$$

where 10^a represents the Hα/Hβ luminosity ratio. We fix the slope to unity, because our JWST sample spans a limited luminosity range and the sample size is small. The best-fit Hα/Hβ luminosity ratios are 4.35 ± 0.26 for the broad components, and 4.41 ± 0.23 for the total luminosity. These values exceed the intrinsic ratio commonly assumed for AGN narrow-line-region (NLR) gas (= 3.1; J. P. Halpern & J. E. Steiner 1983; D. E. Osterbrock & G. J. Ferland 2006) as well as the typical broad-line or total Hα/Hβ ratios of low-redshift quasars (≈ 3.5; e.g., J. E. Greene & L. C. Ho 2005, G. La Mura et al. 2007, J. E. Mejía-Restrepo et al. 2022, S. Son et al. 2025).

These elevated Hα/Hβ ratios are difficult to explain solely by dust attenuation. The mean broad-line ratio implies a V-band extinction of ≈ 1 mag when attributed to dust reddening. Under the extinction curve of the

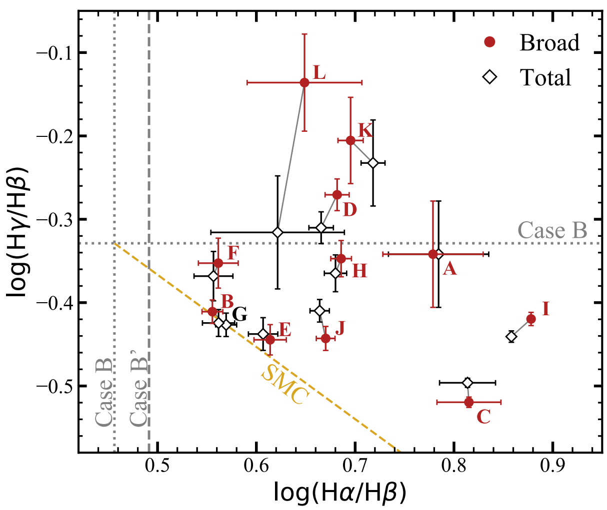

Figure 9. Hα/Hβ and Hγ/Hβ ratios. Red filled circles represent the broad emission lines, while black open diamonds show the total emission lines. Gray dashed lines connect the two measurements for each object. Each object is annotated as in Figure 5. The vertical and horizontal dotted lines indicate the Case B values, while the vertical dashed line shows the intrinsic NLR Balmer decrement of Hα/H$\beta = 3.1$. The orange dashed line indicates the expected line ratios under the SMC extinction curve (Y. C. Pei 1992).

Small Magellanic Cloud (SMC) commonly adopted for quasars (G. T. Richards et al. 2003; P. F. Hopkins et al. 2004; Y. C. Pei 1992), the corresponding attenuation at Lyα wavelength is ≈ 5 mag, which is difficult to reconcile with the detection of broad Lyα emission and the high Lyα luminosities of these objects ($L_{\mathrm{Ly}\alpha} \gtrsim 10^{44}$ erg s^{-1}). Recent JWST studies have suggested that high-redshift sources may have lower A_λ/A_V at UV wavelengths than predicted by local extinction curves (V. Markov et al. 2025), which could reduce the inferred attenuation at Lyα. Nevertheless, an extinction as large as $A_V \approx 1$ mag would remain inconsistent with the blue continuum slopes of these objects discussed in Section 2.5.1. Dust attenuation is therefore unlikely to be the sole origin of the elevated Balmer decrements.

We further illustrate this point in Figure 9, where we compare Balmer decrements measured from different line combinations. The broad Hα/Hβ ratios are generally higher, at a given Hγ/Hβ ratio, than predicted by the SMC extinction curve. This offset suggests that the enhanced Hα/Hβ ratios may reflect non-recombination processes in the dense BLR gas. For example, collisional excitation from the $n = 2$ to the $n = 3$ level can preferentially enhance Hα emission (D. E. Osterbrock & G. J. Ferland 2006). S. Son et al. (2025) also argue that Hα responds less rapidly to continuum variability than Hβ because of its higher optical depth. The enhanced Hα/Hβ ratios of these intermediate-luminosity quasars could partly arise from a decline in the AGN continuum luminosity from a more luminous phase.

The most extreme Balmer decrements are observed in J0844−0132 and J1146−0005, the two LRD-like objects discussed in Section 2.5.1, which both exhibit Hα/H$\beta \approx 7$. These objects are also outliers in the L_{5100} versus $L_{\mathrm{Balmer,broad}}$ relations. Their Balmer decrements are reminiscent of those measured for LRDs, which typically exhibit Hα/H$\beta \approx 8.7$ (A. de Graaff et al. 2026), although J0844−0132 and J1146−0005 do not follow the correlation between L_{5100} and Hα/Hβ reported for their LRDs. Several models have been proposed to explain the extremely high Balmer decrements of LRDs, especially the "black hole star" model, in which young black holes are surrounded by dense gaseous envelopes (K. Inayoshi & R. Maiolino 2025; D. Kido et al. 2025; Z. Yan et al. 2025; A. de Graaff et al. 2026; R. P. Naidu et al. 2025). In this framework, Hβ photons in the envelope undergo repeated resonant scattering and can be converted into Hα and Paα photons, resulting in an enhanced Hα/Hβ ratio. Further investigation, including follow-up observations of reprocessed dust emission, is required to address the origin of their high Balmer decrements and to assess both their similarity to the LRD population and a possible evolutionary connection between the two populations. With these uncertainties in mind, we do not apply dust attenuation corrections to the observed broad-line luminosities of the JWST targets in the following discussion.

Finally, we note that a few objects show Hγ/Hβ ratios higher than the intrinsic value under the Case B recombination. While Hγ is clearly detected in these objects, the lower signal-to-noise ratios of these higher-order transitions, together with the difficulty in modeling the continuum and pseudo-iron emission over a wide wavelength range, may introduce additional systematic uncertainties in the measured line fluxes. We therefore do not overinterpret these elevated Hγ/Hβ ratios. Higher-quality and higher-resolution spectroscopy is required to robustly model weak Balmer lines and decompose them into broad and narrow components.

2.6. *Notes on narrow-line quasars*

Three of the JWST targets analyzed in this paper, J0844−0132, J1146−0005, and J0217−0208, are also included in Y. Matsuoka et al. (2025a), who present JWST/NIRSpec spectroscopy of a subset of the SHELLQs quasars that show relatively narrow Lyα (FWHM < 500 km s^{-1}). About two-thirds of their targets exhibit clear broad components in Balmer emission lines, securing their nature as dust-obscured quasars, while the others are likely dominated by galaxy emission.

We note that the fitting methodology of the NIRSpec spectra is different between this work and Y. Matsuoka et al. (2025a). In their analysis, permitted lines are modeled using three components: narrow, intermediate, and broad. Forbidden lines are modeled using only the narrow and intermediate components, with the line widths and velocity shifts tied across lines within each component. In this framework, the intermediate component is interpreted as galactic outflowing gas, and is seen in [O III] and Hα for all objects, and marginally in [N II]. For J0844−0132 and J1146−0005, this treatment assigns part of the apparently broad Balmer emission to the intermediate component, resulting in narrower broad-line widths by 40–80% than in our fits. Y. Matsuoka et al. (2025a) also correct the quasar emission for dust extinction using the Balmer decrements of the broad-line components, assuming an intrinsic Hα/Hβ ratio of 2.86, when estimating the line luminosities and SMBH properties (see Section 2.5.4). The different fitting methods also affect whether J0217−0208 is interpreted as exhibiting broad emission from the BLR gas. We revisit this model-dependent interpretation of the J0217−0208 spectrum in the next section.

2.7. *Balmer Line Decomposition for J0217−0208*

The line decomposition of J0217−0208 is uncertain because its Balmer emission-line profiles are dominated by narrow lines compared to those of the other JWST targets. Figure 10 shows zoomed-in panels of the decomposed Hβ+[O III] and Hα+[N II] emission-line complexes. Both the Hβ and [O III] doublet emission lines exhibit narrow and broader components. The broader components have FWHM (H$\beta_{\rm broad}$) = 1150 km s^{-1} and FWHM ([O III]wing) = 1160 km s^{-1}, and contribute 23% and 14% of the total line fluxes, respectively. These similar line widths may suggest that the broad Hβ component traces the same outflowing ionized gas as the [O III] wing component.

The middle panel of Figure 10 shows that a broad Hα component is required in our fiducial model. Its FWHM(H$\alpha_{\rm broad}$) $= 1,810$ km s^{-1} is derived without any constraints on its line profile. The right panel of Figure 10 shows an alternative model in which we fix the line width of the broader Hα component to that of the [O III] wing (FWHM = 1160 km s^{-1}), which is a factor of 1.5 narrower than in the fiducial case. We compare the two models using the Bayesian Information Criterion (BIC; G. Schwarz 1978) within $\Delta v = \pm 3,000$ km s^{-1} around Hα and find that the first model yields a smaller BIC (ΔBIC $= -12.1$), favoring a BLR origin rather than an outflow for the broad component. We therefore adopt the broad Hα component as BLR emission in our fiducial interpretation. For consistency with our spectral decomposition, we also use the broad Hβ component to estimate the SMBH properties in the following analysis.

However, the classification of J0217−0208 as a broad-line quasar remains marginal, given the complexity of its line profile and the modest BIC difference between the BLR and outflow models. Y. Matsuoka et al. (2025a) and R. Marques-Chaves et al. (2025) reached different interpretations of the same spectrum using fitting frameworks that include additional Hα and [N II] components associated with outflowing gas, which are not included in our fiducial model. In these frameworks, part of the flux attributed to broad Hα in our model can instead be assigned to an outflow component, making its interpretation model dependent. We nevertheless retain J0217−0208 in our broad-line quasar sample based on our fiducial fitting scheme, while acknowledging that it may instead be a star-forming galaxy with outflowing gas. We also note that this object is included in the analysis of J. D. Silverman et al. (2025). As discussed in Section 4, the Hβ- and Hα-based $M_{\rm BH}$ estimates differ by only 7%, so the choice of mass estimator does not significantly affect the inferred SMBH properties.

3. SUBARU/MOIRCS

In addition to the quasars targeted with JWST, we observed nine SHELLQs quasars in the K_s band with the Multi-Object Infrared Camera and Spectrograph (MOIRCS; T. Ichikawa et al. 2006; R. Suzuki et al. 2008), a Cassegrain instrument on the 8.2 m Subaru telescope. These near-infrared observations enable single-epoch SMBH mass measurements based on the redshifted Mg II emission line. Combined with the sample presented in O19, there are 15 SHELLQs quasars with ground-based near-infrared spectroscopy.

3.1. *Target Selection*

We selected our MOIRCS targets from the SHELLQs sample available at the time of our observations in the S18A–S20B semesters (Y. Matsuoka et al. 2016, 2018a,b). The targets were selected from a sub-sample of the SHELLQs quasars, for which Mg II-based SMBH mass measurements are feasible from the ground. The targets were required to have Lyα redshifts of $z \geq 6.2$ in order to avoid severe atmospheric absorption at the observed wavelength of the Mg II peak. We also imposed an absolute magnitude cut of $M_{1450} \leq -24$, corresponding roughly to the HSC y-band magnitude of $y \leq 23$. This magnitude cut ensures sufficient signal-to-noise ratios for detecting the Mg II emission line with the 8m-class Subaru telescope. We excluded SHELLQs quasars

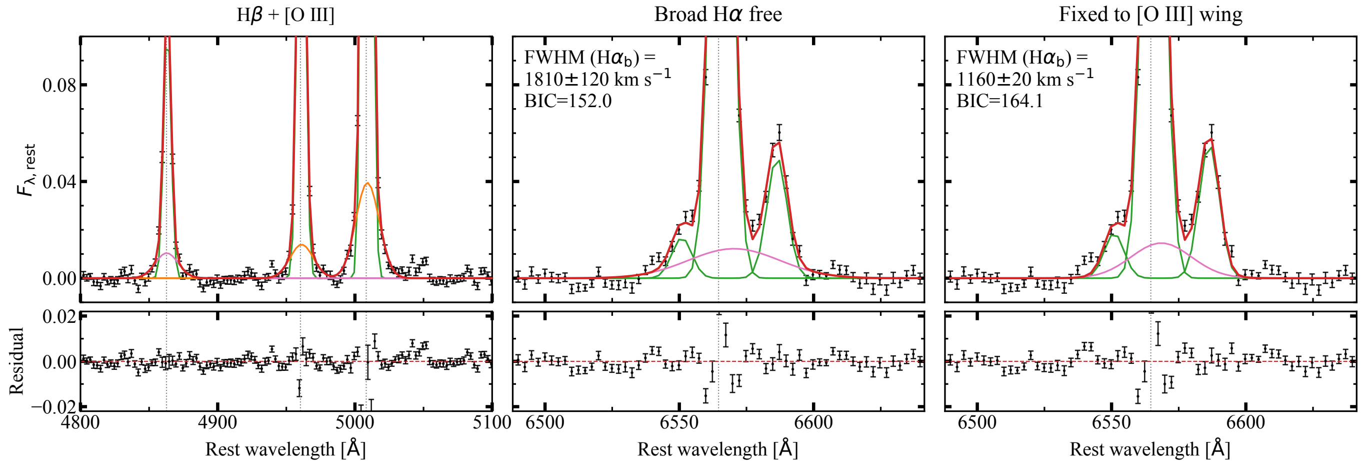

Figure 10. Balmer emission line fitting for J0217−0208. (*Left:*) Hβ+[O III] complex. The line colors are the same as in Figure 3. (*Middle & Right:*) Hα+[N II] complex. The middle panel shows the fit in which broad Hα is modeled without any constraint on its FWHM. The right panel shows the fit in which the FWHM of broad Hα is fixed to that of the [O III] wing. In each panel, the continuum-subtracted spectrum is shown in black, with error bars indicating the 1σ flux uncertainty in each pixel. The broad Hα FWHM and BIC are indicated at the top left of each panel. The bottom panels show the residuals.

that had already been observed with near-infrared spectroscopy in previous studies (M. Onoue et al. 2019; Y. Matsuoka et al. 2019a).

During our observing runs, we prioritized $6.2 \leq z \leq 6.5$ SHELLQs quasars that were used in the study of the $z \sim 6$ quasar luminosity function (Y. Matsuoka et al. 2018c). One of the targets, J1217+0131 at $z = 6.20$, was independently discovered by Pan-STARRS1 (E. Bañados et al. 2016) and the DECam Legacy Survey (F. Wang et al. 2017), and later recovered by our HSC photometric selection (Y. Matsuoka et al. 2018b).

In all, we observed nine SHELLQs quasars with Subaru/MOIRCS. These targets are presented in the second half of Table 1. They occupy the brighter part of this distribution, as shown in Figure 1. In Table 1, we report the PSF magnitudes of these targets in the HSC y-band from the internal DR4 HSC-SSP catalog.

This new sample, together with the previous studies of M. Onoue et al. (2019), C. J. Willott et al. (2010), and Y. Shen et al. (2019), completes the near-infrared spectroscopic coverage of the luminosity-function sample of Y. Matsuoka et al. (2018c) at $6.2 \leq z \leq 6.5$ and $M_{1450} \leq -24$. Follow-up near-infrared spectroscopy remains incomplete at $z > 6.5$. The JWST sample presented in Section 2 covers the fainter SHELLQs quasars in Y. Matsuoka et al. (2018c). We will use this well-defined $z \sim 6$ sample with black hole mass estimates for obtaining the $z \sim 6$ black hole mass function in our future work (Onoue et al. in prep.).

3.2. *K-band spectroscopy*

Our MOIRCS observations, the upgraded 2k × 2k Hawaii 2RG detectors of which were installed in 2015 (J. Walawender et al. 2016; M. Fabricius et al. 2016), were carried out over multiple observing runs: 2018 July 7–8 (Program ID: S18A-061), 2019 April 21–23 (S19A-015), 2020 August 11 (S20B-114) and 2021 January 31 (S20B-114). The observations were performed in the multi-object spectroscopy (MOS) mode for secure acquisition of our faint targets in the narrow MOS slits, guided by bright alignment stars. We chose the VPH-K grism (N. Ebizuka et al. 2011) to cover 2.0 – 2.4 μm at a spectral resolution of $R = 1700$ with a slit width of $0''.8$. We made a custom MOS mask for each target quasar with filler sources and alignment stars. The wavelength coverage of the obtained spectrum of each target depends on the location on the MOS mask. The observations of J1217+0131 were carried out with a preset long-slit mask, for which the target acquisition was performed a blind offset from a nearby star. The total integration time for each target was 0.9–4.5 hours, depending on the faintness and the visibility of the targets during the observing runs. Those integration times were divided into pairs of 240 seconds (S18A and S19A runs) or 300 seconds (S20B) exposures to subtract the time-varying sky background with the standard ABBA nodding offsets. The MOS masks were re-aligned every ~ 1.5 hours to make sure that the targets were at the centers of the target slits during integration.

We also took 5–10 minute Ks-band imaging data of each target during the same run as the spectroscopic observations. We use the Ks-band $2''$-diameter aperture photometry to flux-calibrate the obtained spectrum of each target, so the flux calibration is not affected by potential quasar variability between the spectroscopic and imaging observations. The data reduction of the imaging data used the *MCSALL* task of *MCSRED*[41], the IRAF-based pipeline for MOIRCS imaging data. For each target the photometric zeropoint was determined with field 2MASS stars after converting their 2MASS Ks magnitudes to the Maunakea Observatory filter system based on the prescription of S. K. Leggett et al. (2006). The obtained Ks-band photometry as well as the rest-frame UV continuum slope $\alpha_{\lambda,\rm UV}$ based on HSC y-band and MOIRCS Ks-band photometry are reported in Table 1.

The raw spectroscopic data were reduced in the standard manner using NOAO/IRAF (D. Tody 1986). We rectified the 2D spectra to correct for spectral tilt, and extracted 1D spectra using a Gaussian-weighted aperture. The profile was determined by fitting a Gaussian to each two-dimensional spectrum collapsed along the dispersion direction. At each wavelength bin, the profile center and width were fixed, and only the normalization was scaled to derive the extracted flux. The corresponding error spectra were estimated from the mean sky spectra.

Telluric absorption was corrected using spectra of A-type standard stars observed immediately before or after each science exposure through the same MOS slit as the target quasar. The telluric-corrected one-dimensional spectra were then flux-calibrated by scaling to the MOIRCS K_s-band magnitudes. The spectra were subsequently resampled with a 4 Å step, corresponding to approximately two pixels. Spectra obtained on different observing dates were stacked at this stage. The final reduced spectra are presented in Figure 11.

3.3. *Spectral Fitting*

3.3.1. *Continuum + Iron*

We modeled the obtained K-band spectra of the MOIRCS targets with three components: power-law continuum, the iron emission line forest and the Mg II emission line, following the methodology described in O19. The rest-frame UV continuum from the accretion disk is modeled with a power-law:

$$F_{\lambda,\rm cont} = F_0 \; \lambda^{\alpha_\lambda}, \tag{3}$$

where F_0 is the amplitude and α_λ is the power-law index. The slope of the continuum cannot be well constrained from the MOIRCS spectra alone owing to their narrow wavelength coverage. We instead estimated the slopes from the broad-band photometry at the HSC y-band and the MOIRCS Ks-band, assuming that the broad-band magnitudes are dominated by the continuum. The estimated slope values are reported in Table 1.

Rest-frame iron emission lines are also taken into account as a pseudo-continuum component at rest-frame wavelengths 2000–3000 Å. We use two iron templates in this work: the first from M. Vestergaard & B. J. Wilkes (2001) and the second from Y. Tsuzuki et al. (2006). Both iron templates are based on a high-resolution spectrum of I Zw 1, a local narrow-line Seyfert 1 galaxy. The difference of the two templates and its effect on the Mg II and Fe II measurements have been widely discussed in the literature (e.g., H. Sameshima et al. 2017; J.-H. Woo et al. 2018; M. Onoue et al. 2020; J.-T. Schindler et al. 2020; J. Yang et al. 2021). In short, the Mg II-based single-epoch BH mass measurements are calibrated with the M. Vestergaard & B. J. Wilkes (2001) template, while the template from Y. Tsuzuki et al. (2006) is superior in terms of the accuracy of the Fe II flux beneath the Mg II line and thus the total Mg II flux. As discussed in Section 4, we use the iron template from M. Vestergaard & B. J. Wilkes (2001) in our primary models for BH mass measurements, while we also report our models with the Y. Tsuzuki et al. (2006) template to report accurate Mg II properties. Following J. D. Kurk et al. (2007), we added 20% of the mean continuum flux density at $\lambda_{\rm rest} = 2930$–$2970$ Å to the M. Vestergaard & B. J. Wilkes (2001) template to effectively compensate for the Fe II flux in the Mg II region.

The iron emission was fitted using a grid of broadened iron templates. We convolved the original template with Gaussian kernels to produce templates with FWHM values ranging from 500 to 10,000 km s^{-1} in steps of 500 km s^{-1}. Each template was shifted to the systemic redshift of the quasar based on measurements of [C II] 158 μm when available. J1137+0045, J2304+0045, J1406−0116, and J1217+0131 were observed and analyzed in Sawamura, M. et al. (*in prep.*), and J0921+0007 was observed in F. Wang et al. (2024). If [C II] observations were not available (J2210+0304, J1545+4232, J1350−0027, J1004+0239), we used Lyα redshifts as an initial guess of the systemic redshifts and iteratively updated them using the Mg II redshifts. For each assumed iron template, we alternately fitted the continuum model and the iron emission until the scale factor of the iron template converged ($< 1\%$), following the description of M. Vestergaard & B. J. Wilkes (2001). We then adopted the model with the minimum χ^2 among the converged fits as the best-fit iron model. We do not consider the iron component for J1350−0027, which shows a noisy spectrum, and instead use a constant continuum model.

[41] The software was developed by Ichi Tanaka: https://www.naoj.org/staff/ichi/MCSRED/mcsred.html

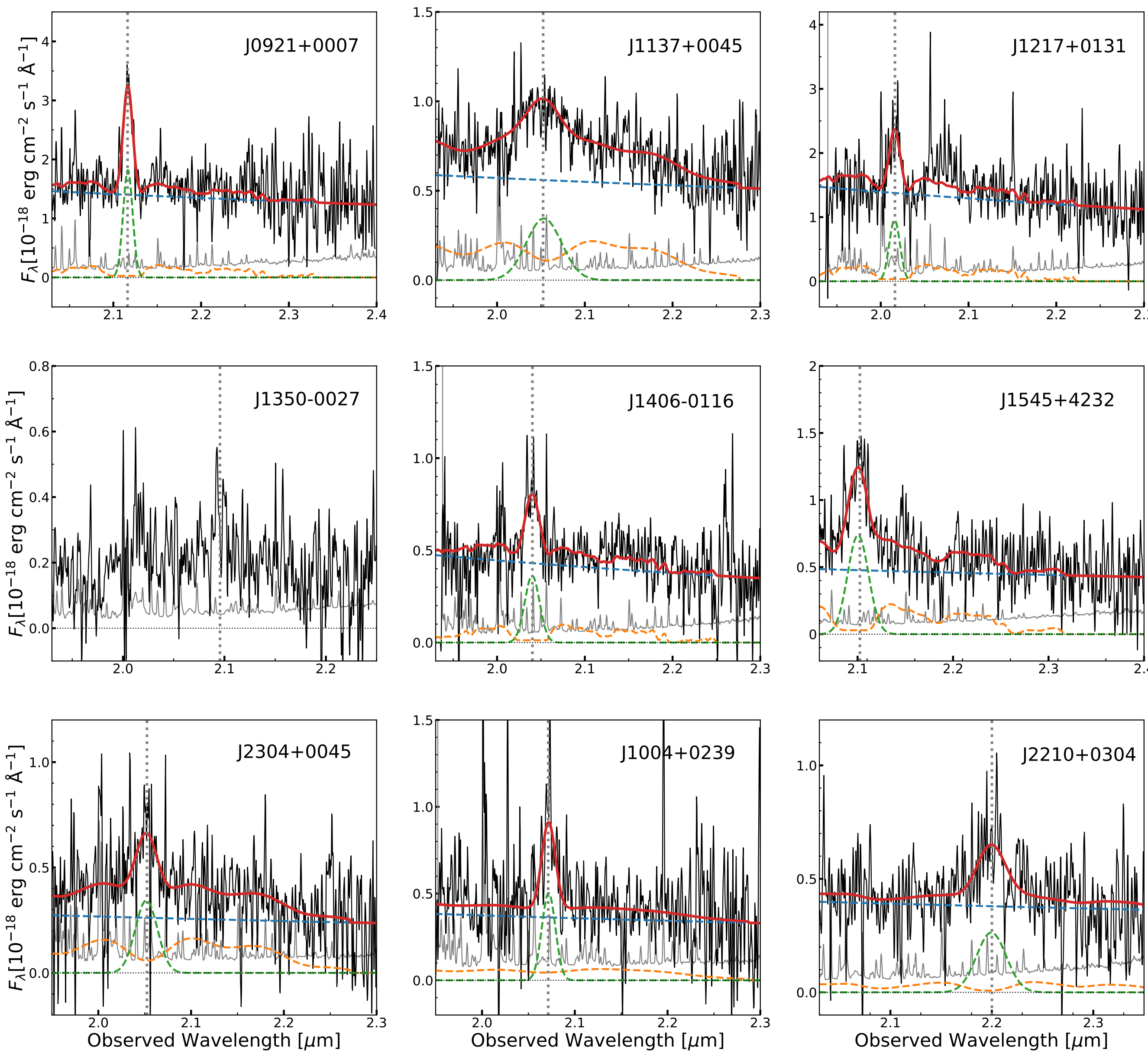

Figure 11. The K-band spectra of the 9 MOIRCS targets (black). For visualization purposes, the spectrum in each panel is smoothed using a Gaussian kernel with $\sigma = 2$ pixels. The noise spectrum is shown in grey. The best-fit power-law continuum, iron, and Mg II emission line models are shown as blue, orange, and green dashed curves, respectively, and their sum is shown as solid red curves. The iron model in this figure is based on the I Zw 1 template by M. Vestergaard & B. J. Wilkes (2001). The vertical black dotted lines show the expected Mg II centers from their systemic redshifts. The fitting model for J1350−0027, which shows an absorption feature at the line peak, is presented in Figure 12.

3.3.2. *Mg II Line Fitting*

The Mg II emission line properties of each quasar were measured after subtracting the best-fit power-law+iron continuum model. We detected significant flux excess for all targets at the wavelengths close to where Mg II are expected based on the optical and [CII] redshifts. We fitted a single Gaussian profile for each spectrum to measure the amplitude, central wavelength and line width. The Mg II line of J1350−0027 was modeled as resolved Mg II $\lambda\lambda2797, 2803$ doublet emission using two Gaussian components with a common FWHM (See Section 3.4).

The uncertainties of the continuum and emission line parameters are measured by Monte Carlo resampling.

Table 5. Mg II line properties for the MOIRCS targets

ID	$z_{\rm MgII}$	L_{3000}	FWHM(Mg II)	$L_{\rm MgII}$
		[10^{45} erg s^{-1}]	[km s^{-1}]	[10^{43} erg s^{-1}]
J2210+0304	$6.859^{+0.006}_{-0.005}$	4.7 ± 0.4	4700^{+800}_{-900}	$5.3^{+0.9}_{-0.7}$
J0921+0007	$6.562^{+0.001}_{-0.001}$	14.5 ± 0.5	1800^{+100}_{-100}	$12.1^{+1.3}_{-0.8}$
J1545+4232	$6.505^{+0.002}_{-0.002}$	4.9 ± 0.3	3700^{+200}_{-200}	$9.8^{+0.7}_{-0.6}$
J1350−0027	6.49	2.3 ± 0.1	370^{+60}_{-100}	$0.73^{+0.10}_{-0.12}$
J1004+0239	$6.402^{+0.003}_{-0.003}$	3.5 ± 0.2	2500^{+1100}_{-300}	$4.3^{+1.1}_{-0.4}$
J1137+0045	$6.347^{+0.004}_{-0.003}$	3.1 ± 0.2	6800^{+200}_{-300}	$12.0^{+0.4}_{-0.5}$
J2304+0045	$6.331^{+0.005}_{-0.004}$	2.5 ± 0.1	4100^{+300}_{-600}	$4.6^{+0.3}_{-0.4}$
J1406−0116	$6.289^{+0.003}_{-0.003}$	3.7 ± 0.1	2900^{+200}_{-300}	$3.4^{+0.4}_{-0.3}$
J1217+0131	$6.202^{+0.003}_{-0.003}$	11.5 ± 0.2	2100^{+200}_{-200}	$6.3^{+0.8}_{-0.8}$

NOTE— The line properties reported here are based on M. Vestergaard & B. J. Wilkes (2001) iron template. The same table for the case when we use Y. Tsuzuki et al. (2006) iron template is reported in Appendix A. L_{3000} is the monochromatic luminosity at rest-frame 3000 Å in the unit of 10^{45} erg s^{-1}. The Mg II emission line of J1350−0027 is fitted with two Gaussian profiles (see main text for details).

From each unsmoothed flux-calibrated spectrum, 1,000 mock spectra are generated by adding random noise to each spectral pixel based on its noise vector. The mock spectrum is then smoothed by the same Gaussian kernels and the power-law+iron+Mg II fitting was repeated with the procedure described in Section 3.3.1. The 1σ uncertainty is given by 16% and 84% percentiles of the distribution of the best-fit values. The derived emission line properties including the redshift measurements are shown in Table 5.

We tested with the five objects with available [C II] to fit the spectra with and without fixing the iron templates to [C II] redshifts. We find that the resulting Mg II line widths change by only $< 1\%$: therefore, we confirm that the availability of [C II] redshift does not significantly affect our line measurements.

3.4. *Notes on Individual Objects*

J0921+0007: This quasar exhibits a relatively narrow Mg II emission line with FWHM $= 1700 \pm 100$ km s^{-1}. It is marginally detected in rest-frame hard X-ray observations, $L_{2-10\ \rm kev} = (2.96 \pm 1.71) \times 10^{45}$ erg s^{-1}, by the extended ROentgen Survey with an Imaging Telescope Array (eROSITA), later confirmed by deeper Chandra observations (J. Wolf et al. 2023). Its X-ray loudness relative to rest-frame ultraviolet luminosity makes it a high-redshift analog of a local Seyfert 1 galaxy. The Eddington ratio of J0921+0007 is among the highest among our SHELLQs sample (See Section 4.1).

J1350−0027: This quasar is the faintest in Ks-band among our MOIRCS targets (22.48 ± 0.14 mag). Figure 11 shows that J1350−0027 exhibits a double-peaked feature at Mg II. This line profile may arise from either resolved Mg II $\lambda\lambda 2797, 2803$ doublet emission or broad Mg II absorption imprinted on an underlying broad emission component (e.g., P. B. Hall et al. 2002; H. Choi et al. 2022).

Figure 12 shows unbinned Ks-band spectrum of this source, in which Mg II is reasonably well modeled with a resolved doublet emission model. The measured line FWHM of 370^{+60}_{-100} km s^{-1} is 40% narrower than that of Lyα (620 ± 200 km s^{-1}; Y. Matsuoka et al. 2019b). Within the SHELLQs sample, this object lies at the boundary of the definition of "narrow-line" quasars, namely Lyα FWHM < 500 km s^{-1} (Y. Matsuoka et al. 2019b). Y. Matsuoka et al. (2025a) showed from JWST rest-optical spectroscopy that this sub-population consists of a mixture of dust-reddened broad-line quasars and galaxies. These objects may also be related to the LRD population identified by JWST.

It is therefore possible that J1350−0027 is a dust-reddened quasar, similar to those reported by Y. Matsuoka et al. (2025a), in which only narrow emission lines from ionized gas in NLR are visible in the rest-frame ultraviolet (M. Onoue et al. 2021). However, given the low signal-to-noise ratio of the Mg II spectrum and the ab-

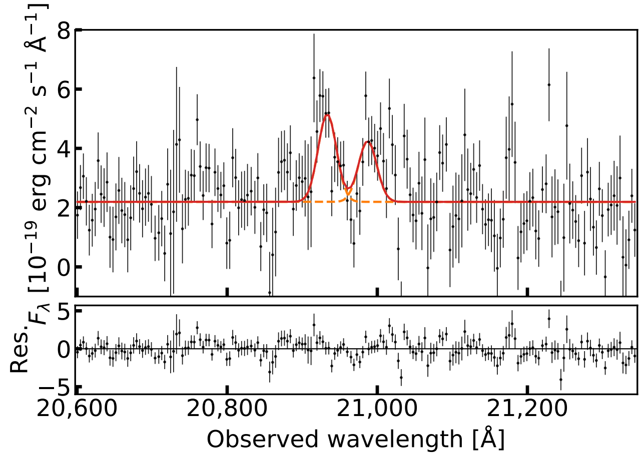

Figure 12. The unsmoothed spectrum of J1350−0027. The spectrum is modeled assuming that the observed double–peaked feature corresponds to resolved Mg II $\lambda\lambda 2797, 2803$ doublet emission. Orange dashed curves indicate the two Gaussian components, and the red solid curve shows the combined model including a constant continuum. The residuals are shown in the bottom panel.

sence of JWST spectroscopy currently available for this object, we cannot reliably distinguish between the dust-obscured quasar scenario and the low-ionization broad absorption line quasar scenario. We therefore exclude J1350−0027 from the subsequent statistical analysis of the SHELLQs broad-line quasars.

4. BH MASS AND EDDINGTON RATIO

Assuming that the BLR gas is gravitationally bound to the central black hole, the virial SMBH mass is given by:

$$M_{\rm BH} = fG^{-1}v_{\rm BLR}^2 R_{\rm BLR}, \quad (4)$$

where G is the gravitational constant, $v_{\rm BLR}$ is the circular velocity of the BLR gas, and $R_{\rm BLR}$ is its distance from the black hole. The amplitude f takes into account the geometry of the BLR gas. In practice, these relations are implemented using the FWHM or velocity dispersion of broad emission lines as a proxy for $v_{\rm BLR}$, together with the continuum luminosity to estimate $R_{\rm BLR}$ via the BLR size-luminosity relation calibrated against reverberation mapping studies (S. Kaspi et al. 2000; M. Vestergaard 2002; M. Vestergaard & B. M. Peterson 2006; Y. Shen et al. 2024).

We use Balmer emission lines to estimate SMBH masses for our JWST targets. M. Vestergaard & B. M. Peterson (2006) calibrate the Hβ-based $M_{\rm BH}$ as

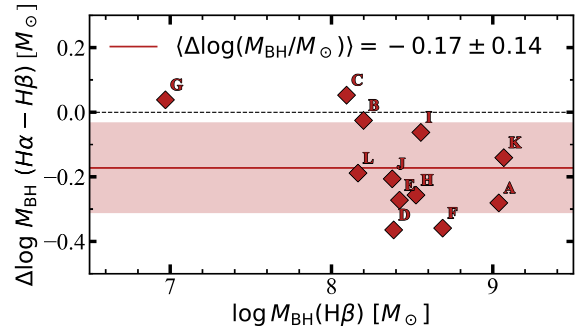

Figure 13. Comparison of the Hβ-based and Hα-based $M_{\rm BH}$ for the JWST targets. Each object is annotated as in Figure 5. The y-axis represents the difference between the Hα- and Hβ-based $M_{\rm BH}$. The mean offset and the 1σ scatter are shown by the red line and shaded region, respectively.

$$M_{\rm BH} = 8.1{\times}10^6 \left(\frac{\rm FWHM\ (H\beta)}{10^3\ [\rm km\ s^{-1}]}\right)^2 \left(\frac{L_{5100}}{10^{44}\ [\rm erg\ s^{-1}]}\right)^{0.5} M_\odot, \quad (5)$$

where FWHM (Hβ) is the full width at half maximum of the broad Hβ line, and L_{5100} is the monochromatic luminosity at rest-frame 5100 Å. We note that the observed 5100 Å continuum luminosities of our JWST targets ($\sim 10^{45}$ erg s^{-1}) are well covered by the local sample of M. Vestergaard & B. M. Peterson (2006). The measurement uncertainties of the virial black hole masses are derived by propagating the measurement errors of the line widths and the continuum model. These uncertainties are smaller than the systematic uncertainty of ~ 0.4 dex inherent to single-epoch virial mass estimates (Y. Shen 2013; Y. Shen et al. 2024).

Alternatively, we apply the virial SMBH mass recipe of J. E. Greene & L. C. Ho (2005), which is based on the broad Hα line width and luminosity:

$$M_{\rm BH} = 2.0{\times}10^6 \left(\frac{\rm FWHM\ (H\alpha)}{10^3\ [\rm km\ s^{-1}]}\right)^{2.06} \left(\frac{L_{\rm H\alpha}}{10^{42}\ [\rm erg\ s^{-1}]}\right)^{0.55} M_\odot. \quad (6)$$

This widely-used $M_{\rm BH}$ recipe leverages the tight correlation between L_{5100} and $L_{\rm H\alpha}$ of their local sample, which makes it possible to estimate $M_{\rm BH}$ solely from Hα. These Hβ- and Hα-based $M_{\rm BH}$ are summarized in the bottom half of Table 6.

Figure 13 compares the $M_{\rm BH}$ measurements based on Hβ (Equation 5) and Hα (Equation 6). We find modest offsets of the Hα-based $M_{\rm BH}$ with $\Delta\log M_{\rm BH} = \log M_{\rm BH}(H\beta) - \log M_{\rm BH}(H\alpha) = -0.17 \pm 0.14$. This systematic offset is explained by the difference in the L_{5100}–$L_{\rm H\alpha}$ correlation between $z \sim 6$ and low redshift (Figure 7), as well as by the different BLR geometries assumed in the two $M_{\rm BH}$ recipes (see, e.g., J.-H. Woo et al. 2015; J. E. Mejía-Restrepo et al. 2022, for detailed discussions). Nevertheless, the estimated masses are broadly consistent within the typical systematic uncertainty of single-epoch estimates (~ 0.4 dex; Y. Shen 2013), and this small offset does not alter our key findings (Section 4.4).

For the Mg II-based SMBH mass estimates of the MOIRCS targets, we adopt the prescription of M. Vestergaard & P. S. Osmer (2009):

$$M_{\rm BH} = 7.2\times10^6 \left(\frac{\rm FWHM\ (Mg\,II)}{10^3\ [\rm km\ s^{-1}]}\right)^2 \left(\frac{L_{3000}}{10^{44}\ [\rm erg\ s^{-1}]}\right)^{0.5} [M_\odot] \quad (7)$$

where FWHM (Mg II) is the full width at half maximum of the Mg II line, and L_{3000} is the monochromatic luminosity at rest-frame 3000 Å.

We use the Mg II line width measurements from the line fitting with the M. Vestergaard & B. J. Wilkes (2001) iron template, to be consistent with O19 and other similar works in the literature. These $M_{\rm BH}$ estimates based on Mg II emission lines are summarized in the first half of Table 6. The case when the Y. Tsuzuki et al. (2006) iron template is used is presented in Appendix A. In addition, we will discuss the impact of the choice of different $M_{\rm BH}$ calibration in Section 4.4.

The luminosity-based Eddington ratios $L_{\rm bol}/L_{\rm Edd}$ of our NIRSpec and MOIRCS targets are presented in Table 6. For this purpose, the Eddington luminosity is given by $L_{\rm Edd} = 1.3 \times 10^{38}\,(M_{\rm BH}/M_\odot)$ erg s^{-1}. The Hβ-based $M_{\rm BH}$ is used for the JWST targets. The bolometric luminosity $L_{\rm bol}$ is estimated by scaling the UV or optical continuum luminosity of each target, adopting the standard bolometric corrections for quasars presented in G. T. Richards et al. (2006). For the JWST targets, we use the host-subtracted 5100 Å luminosity,

$$L_{\rm bol} = 9.26\ L_{\rm 5100,QSO}\ [\rm erg\ s^{-1}]. \quad (8)$$

For the MORICS targets, we use the 3000 Å luminosity,

$$L_{\rm bol} = 5.15\ L_{3000}\ [\rm erg\ s^{-1}]. \quad (9)$$

Finally, we note that our SHELLQs quasars have either Mg II or Balmer line observations, but none of them has both. This is partly because the JWST targets in this study are too faint for ground-based Mg II spectroscopy. Early high-redshift JWST studies have shown overall agreement between Mg II- and Hβ-based $M_{\rm BH}$ estimates, although offsets of up to ~ 0.5 dex have been reported for individual objects (A.-C. Eilers et al. 2023; J. Yang et al. 2023; J. Lyu et al. 2025). Such differences are, however, comparable to the typical uncertainties of single-epoch mass estimates (Y. Shen 2013). It therefore remains unclear whether these BLR emission lines trace the same BLR kinematics as in the local universe and whether locally calibrated single-epoch $M_{\rm BH}$ estimators can be reliably applied at high redshift.

4.1. *Distribution of $M_{\rm BH}$ and $L_{\rm bol}/L_{\rm Edd}$*

The redshift dependence of BH mass and Eddington ratio distributions provides insight into the growth history of SMBHs over cosmic time. The fraction of SMBHs accreting at super-Eddington rates holds the key to explaining the existence of billion-solar-mass BHs at high redshift (e.g., T. Kawaguchi et al. 2004; M. Volonteri et al. 2015; H. Shirakata et al. 2019; W. Li et al. 2023; A. Lupi et al. 2024; K. Inayoshi & R. Maiolino 2025).

There are 27 SHELLQs quasars in total, including 12 objects with Hβ-based measurements obtained in this work and 15 objects with Mg II-based black hole mass measurements from this work and previous near-infrared observations (M. Onoue et al. 2019; Y. Matsuoka et al. 2019a; N. Kato et al. 2020). These SHELLQs quasars span a bolometric luminosity range of $46 \lesssim \log L_{\rm bol}\ [\rm erg\ s^{-1}] \lesssim 47$ and occupy an intermediate regime between classical luminous quasars (e.g., J. Yang et al. 2023; M. Yue et al. 2024) and faint broad-line AGN recently identified by JWST (e.g., R. Maiolino et al. 2024; I. Juodžbalis et al. 2026).

The left panel of Figure 14 shows the distribution of black hole mass and bolometric luminosity for the 27 SHELLQs quasars. The right panel shows the corresponding distribution of Eddington ratios. For comparison, we also show in both panels luminous $z > 6$ quasars with Balmer-line-based $M_{\rm BH}$ measurements (J. Yang et al. 2023; A.-C. Eilers et al. 2023; M. Yue et al. 2024) and faint broad-line AGNs identified by the JWST JADES program (I. Juodžbalis et al. 2026).

The single-epoch black hole masses of the SHELLQs quasars span a wide range of $7.0 \le \log(M_{\rm BH}/M_\odot) \le 9.5$, with a median of $\langle\log(M_{\rm BH}/M_\odot)\rangle = 8.6$. The Eddington ratios of the SHELLQs quasars range from $-1.2 \le \log(L_{\rm bol}/L_{\rm Edd}) \le 0.3$, with a median of $\langle\log(L_{\rm bol}/L_{\rm Edd})\rangle = -0.6$. The side histograms in Figure 14 show that the $M_{\rm BH}$ and $L_{\rm bol}/L_{\rm Edd}$ of the SHELLQs quasars are systematically shifted toward lower $M_{\rm BH}$ and higher $L_{\rm bol}/L_{\rm Edd}$ than those of the luminous quasars. This trend also holds when the SHELLQs sample is compared to the Mg II-based $M_{\rm BH}$ measurements available in the literature at $z \gtrsim 6$ (e.g., C. J. Willott et al. 2010; C. Mazzucchelli et al. 2017, 2023; Y. Shen et al. 2019; J. Yang et al. 2021; E. P. Farina et al. 2022). For example, E. P. Farina et al. (2022) show that the median $M_{\rm BH}$ and $L_{\rm bol}/L_{\rm Edd}$ of their XQR-30 sample

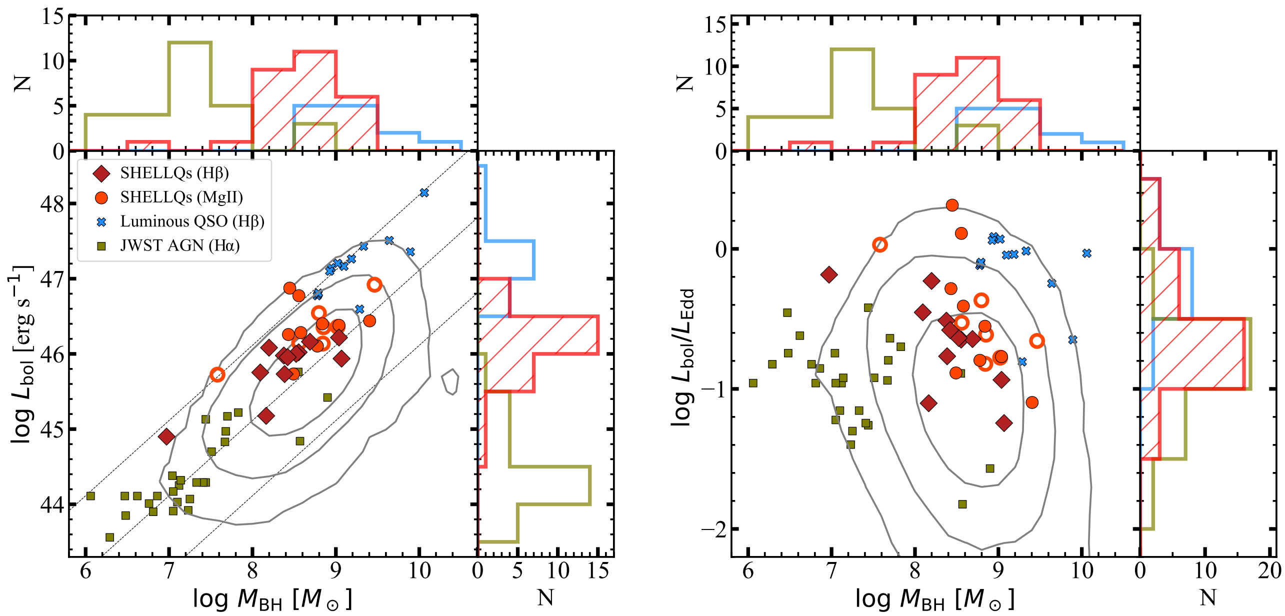

Figure 14. (*Left*) Black hole mass–bolometric luminosity distribution at $z \sim 6$–7. SHELLQs quasars with JWST-based Hβ $M_{\rm BH}$ measurements are shown as red diamonds, while those with Mg II-based $M_{\rm BH}$ are shown as orange circles. Filled symbols indicate the SHELLQs quasars observed by MOIRCS in this work, whereas open symbols are taken from O19 and N. Kato et al. (2020). For the JWST targets in this work, the host-galaxy contribution to the 5100 Å luminosity has been subtracted based on the NIRCam decomposition analysis of X. Ding et al. (2025). Hβ-based $M_{\rm BH}$ measurements for $z > 6$ luminous quasars from the literature are shown as blue crosses (J. Yang et al. 2023; A.-C. Eilers et al. 2023; M. Yue et al. 2024) . Hα-based faint JWST AGN from I. Juodžbalis et al. (2026) are shown as green squares. The background contours show the density distribution of $z \approx 1$–2 SDSS DR16Q quasars (Q. Wu & Y. Shen 2022), enclosing 68%, 95%, and 99.7% of the population, restricted to objects with Mg II-based black hole mass estimates (Section 4.2). Their bolometric luminosities and black hole masses are derived using the same prescriptions as those adopted for the high-redshift samples. The diagonal lines indicate Eddington ratios of $L_{\rm bol}/L_{\rm Edd} = 1$, 0.1, and 0.01 from left to right. The upper and right panels show the black hole mass and bolometric luminosity distributions, respectively. The orange histograms show the distributions of the full SHELLQs targets, combining the JWST and ground-based samples. (*Right*) The corresponding SMBH mass – Eddington ratio distribution for the same samples.

at $L_{\rm bol} > 2.9 \times 10^{46}$ erg s^{-1} are $\langle \log(M_{\rm BH}/M_\odot)\rangle = 9.5$ and $\langle \log(L_{\rm bol}/L_{\rm Edd})\rangle = -0.32$, respectively. Thus, compared to the more luminous quasar population, the SHELLQs quasars trace SMBHs in an earlier and more active phase of their growth in the early universe.

While we are now identifying sub-Eddington SMBHs that are as massive as those powering typical luminous quasars ($\log M_{\rm BH}/M_\odot \sim 9$), thanks to the deep imaging of the HSC-SSP, we do not find any at $\log M_{\rm BH}/M_\odot \sim 10$, although the depth of the HSC-SSP should be able to detect such SMBHs if they accrete at $\gtrsim 1\%$ Eddington. Such ultramassive SMBHs are known to exist at $z \sim 6$ (O. Shemmer et al. 2004; H. Netzer et al. 2007; X.-B. Wu et al. 2015), although they are intrinsically rare. Their absence from the HSC-SSP sample may therefore be primarily due to the smaller sky coverage of HSC-SSP (1,100 deg^2) compared to SDSS (15,000 deg^2), together with the incomplete SMBH mass measurements for the SHELLQs quasars. Also, such rarest $\log M_{\rm BH}/M_\odot \sim 10$ systems will likely be found in the $\gtrsim 2,000$ deg^2 wide-area surveys of Euclid and Roman.

At the opposite end of the Eddington-ratio distribution, three out of 27 (i.e., 11%) of the $z \sim 6$ SHELLQs quasars show accretion rates higher than the Eddington limit, albeit with systematic uncertainties of 0.4 dex in individual $M_{\rm BH}$ estimates. Those are J0921+0007 and J1217+0131 in this study, and J0859+0052 in O19, which all have MgII-based $M_{\rm BH}$. Remarkably, one of these objects, J0921+0007 is detected in X-rays (J. Wolf et al. 2023) despite the fact that its rest-frame ultraviolet luminosity is ≈ 1 dex fainter than other X-ray bright $z > 6$ quasars (R. Nanni et al. 2017). Existence of super-Eddington SMBHs at high redshift has been reported in the literature (L. Jiang et al. 2007; C. J. Willott et al. 2010; E. Bañados et al. 2021; F. Wang et al. 2021; J. Yang et al. 2021; E. P. Farina et al. 2022; C. Mazzucchelli et al. 2023). Specifically, C. J. Willott et al. (2010) reported that about half of their nine quasars at com-

Table 6. Black Hole Mass Estimates

ID	$M_{\rm BH,H\beta}$	$M_{\rm BH,H\alpha}$	$M_{\rm BH,Mg\,II}$	$L_{\rm bol}/L_{\rm Edd}$	$L_{\rm bol}$
	$[10^8 M_\odot]$	$[10^8 M_\odot]$	$[10^8 M_\odot]$		$[10^{45}$ erg s$^{-1}]$
			JWST/NIRSpec		
J2255+0251	1.58 ± 0.06	1.49 ± 0.05	⋯	0.590 ± 0.023	12.12 ± 0.08
J2236+0032	10.90 ± 2.86	5.71 ± 0.21	⋯	0.116 ± 0.031	16.47 ± 0.11
J0844−0132	3.58 ± 0.09	3.10 ± 0.04	⋯	0.225 ± 0.005	10.46 ± 0.03
J0844−0052	4.89 ± 0.41	2.14 ± 0.09	⋯	0.227 ± 0.019	14.46 ± 0.11
J0918+0139	3.34 ± 0.23	1.85 ± 0.05	⋯	0.231 ± 0.016	10.02 ± 0.06
J1425−0015	2.38 ± 0.08	1.48 ± 0.04	⋯	0.307 ± 0.011	9.51 ± 0.07
J1525+4303	2.43 ± 0.11	1.05 ± 0.03	⋯	0.171 ± 0.008	5.39 ± 0.05
J1146−0005	1.24 ± 0.07	1.40 ± 0.53	⋯	0.352 ± 0.019	5.66 ± 0.01
J1146+0124	2.64 ± 0.16	1.41 ± 0.12	⋯	0.263 ± 0.016	9.04 ± 0.04
J0217−0208	0.0934 ± 0.0002	0.10 ± 0.01	⋯	0.654 ± 0.004	0.794 ± 0.004
J1512+4422	11.70 ± 0.49	8.46 ± 0.03	⋯	0.057 ± 0.002	8.65 ± 0.04
J0911+0152	1.46 ± 0.45	0.95 ± 0.04	⋯	0.079 ± 0.025	1.50 ± 0.01
			Subaru/MOIRCS		
J2210+0304	⋯	⋯	$10.90^{+5.52}_{-4.95}$	$0.17^{+0.14}_{-0.06}$	24.0 ± 1.6
J0921+0007	⋯	⋯	$2.81^{+0.41}_{-0.31}$	$2.05^{+0.29}_{-0.34}$	74.9 ± 2.8
J1545+4232	⋯	⋯	$6.86^{+0.72}_{-0.82}$	$0.28^{+0.04}_{-0.04}$	25.1 ± 1.5
J1004+0239	⋯	⋯	$2.65^{+1.82}_{-0.87}$	$0.52^{+0.26}_{-0.21}$	18.1 ± 0.9
J1137+0045	⋯	⋯	$25.40^{+2.38}_{-3.71}$	$0.08^{+0.01}_{-0.01}$	27.5 ± 1.0
J1406−0116	⋯	⋯	$3.79^{+0.61}_{-0.70}$	$0.39^{+0.09}_{-0.06}$	19.2 ± 0.5
J2304+0045	⋯	⋯	$6.03^{+1.77}_{-1.65}$	$0.16^{+0.06}_{-0.04}$	12.7 ± 0.6
J1217+0131	⋯	⋯	$3.55^{+0.69}_{-0.73}$	$1.29^{+0.34}_{-0.20}$	59.4 ± 1.2

NOTE— The uncertainties of the SMBH mass estimate reported here do not include 0.4 dex of intrinsic scatter of the virial $M_{\rm BH}$ estimates (Y. Shen 2013). For JWST targets, Hβ-based $M_{\rm BH}$ is based on the host subtracted 5100 Å luminosity $L_{\rm 5100,QSO}$. The Eddington ratio $L_{\rm bol}/L_{\rm Edd}$ are based on the Hβ-based $M_{\rm BH}$. The bolometric luminosities $L_{\rm bol}$ are from $L_{\rm 5100,QSO}$ and L_{3000} for JWST and MOIRCS targets, respectively.

parable M_{1450} to our MOIRCS targets accrete at super-Eddington rates ($L_{\rm bol}/L_{\rm Edd} > 1$). In Section 4.4, we discuss the possibility that the fraction of super-Eddington SMBHs in our sample may be even higher.

4.2. *Comparison with $M_{\rm BH}$ and $L_{\rm bol}/L_{\rm Edd}$ at Lower redshifts*

Previous studies have investigated the distributions of BH mass and Eddington ratio for luminous quasars at $\log L_{\rm bol}$ [erg s^{-1}] $\gtrsim$ 47 (e.g., C. J. Willott et al. 2010; J. Yang et al. 2021; E. P. Farina et al. 2022; C. Mazzucchelli et al. 2023); however, such luminous quasar samples are naturally biased toward most massive and rapidly accreting SMBHs. Here we compare the BH mass and Eddington ratio distributions of the intermediate-luminosity SHELLQs sample with those of a low-redshift control sample to investigate whether the accretion properties of SMBHs evolve with redshift.

For the control sample at low redshift, we use the spectral measurements for the sixteenth data release of Sloan Digital Sky Survey quasar catalog (B. W. Lyke et al. 2020). We select quasars for which Mg II-based black hole mass estimates are available in Q. Wu & Y. Shen (2022). The mean redshift of this low-redshift sample is $z = 1.3$. We do not use quasars with Hβ-based black hole masses for the control sample, because only a small number of such objects exist at bolometric luminosities $L_{\rm bol} > 10^{46.5}$ erg s^{-1}.

We perform Monte Carlo resampling of the low-redshift quasars. In each realization, 27 objects are randomly drawn with replacement, such that each low-redshift object is matched in $L_{\rm bol}$ to one of the high-redshift quasars within ± 0.1 dex. We calculate $M_{\rm BH}$, $L_{\rm bol}$, and $L_{\rm bol}/L_{\rm Edd}$ for the extracted low-redshift quasars following the same method as for the high-redshift sample (Equations 7, 9). We then compare the luminosity-matched low-redshift distribution with the high-redshift sample. An ensemble of 10,000 realizations is used to derive the average distributions, thereby accounting for sample variance and uncertainties in the matching procedure.

Figure 15 presents the black hole mass and Eddington ratio distributions of both the high-redshift sample and the luminosity-matched low-redshift quasar sample described above. We obtain a median black hole mass of $\log(M_{\rm BH}/M_{\odot}) = 8.91^{+0.33}_{-0.37}$ for the low-redshift quasars, where the quoted uncertainties represent the 16th–84th percentile range. The scatter of the median $M_{\rm BH}$ between different realizations is 0.08 dex, which is smaller than the spread of the distribution. The corresponding median Eddington ratio is $\log(L_{\rm bol}/L_{\rm Edd}) = -0.85^{+0.33}_{-0.36}$. We find that the median black hole mass of the high-redshift sample is offset by $\Delta \log(M_{\rm BH}/M_{\odot}) = -0.35$ with respect to the low-redshift sample. Likewise, the high-redshift sample has a higher accretion efficiency, with a mean offset of $\Delta \log(L_{\rm bol}/L_{\rm Edd}) = 0.23$. Therefore, SMBH accretion activity is systematically more efficient at $6 < z < 7$ than at lower redshifts, suggesting that the trend previously found for luminous quasars extends to the more representative high-redshift SMBH population.

It is also remarkable that the high-redshift sample exhibits an extended tail toward the super-Eddington regime ($L_{\rm bol}/L_{\rm Edd} \gtrsim 1$) and a relative deficit of Eddington ratios below 5% Eddington. This trend is unlikely to be driven by observational biases, as both the high- and low-redshift quasar samples discussed here were selected based on luminosity, and not by Eddington ratio. In order to address this apparent trend, we apply the Anderson–Darling (AD) test (T. W. Anderson & D. A. Darling 1952), which is sensitive to differences in distribution tails, to test the null hypothesis that the black hole mass and Eddington ratio distributions between the low- and high-redshift samples are drawn from the same underlying parent distribution. We perform the AD test for each Monte Carlo realization of the low-redshift sample. We obtain a median p-value of 0.007, with the null hypothesis rejected ($p < 0.05$) in 87.2% of the random realizations, indicating that the difference between the high- and low-redshift quasar samples persists for the majority of the luminosity-matched low-redshift samples. This result suggests that the enhanced fraction of rapidly accreting SMBHs at high redshift contributes to the observed difference from the low-redshift population. This result suggests that the enhanced fraction of rapidly accreting SMBHs at high redshift contributes to the observed difference from the low-redshift population.

The excess of super-Eddington objects and the overall enhancement of the SMBH accretion activity in the high-redshift sample is relevant to the so-called AGN downsizing discussed in X-ray AGN studies, in which the most rapidly accreting and luminous black holes reach their peak activity at higher redshifts (Y. Ueda et al. 2003; A. Merloni 2004). Such a picture has also been indicated by theoretical studies of distant SMBHs (P. Madau et al. 2014; H. Shirakata et al. 2019; K. Inayoshi et al. 2020; A. Lupi et al. 2024). In this context, our result extends the downsizing picture from the most luminous quasar population to a more representative population at the epoch of reionization.

4.3. *Possible Bias in MOIRCS $M_{\rm BH}$ Estimates*

We assess the impact of the modest quality of the MOIRCS spectra on the Mg II-based virial SMBH mass

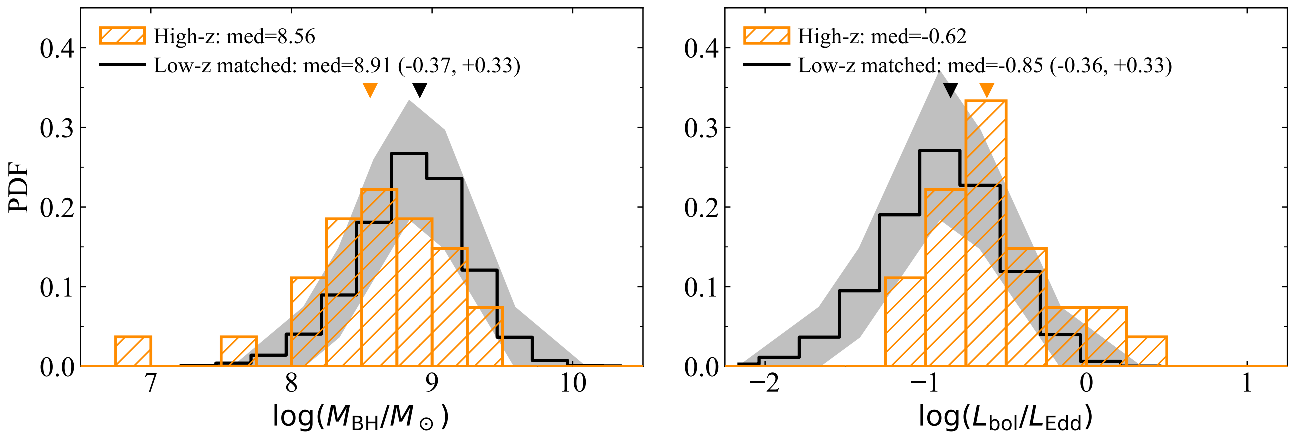

Figure 15. Distribution of black hole mass (left) and Eddington ratio (right) of the 27 SHELLQs quasars at $z \sim 6$–7 (orange) and the luminosity-matched SDSS DR16 quasars at $z \approx 1.3$ (black). The low-redshift sample is extracted from Monte Carlo resampling to reproduce the $L_{\rm bol}$ distribution of the high-redshift sample. The black histogram shows the median probability distribution function (PDF) in each $\log M_{\rm BH}/M_\odot$ or $\log L_{\rm bol}/L_{\rm Edd}$ bin over the Monte Carlo realizations, while the grey shaded area indicates the 16–84 percentile. The median $\log(M_{\rm BH}/M_\odot)$ and $\log(L_{\rm bol}/L_{\rm Edd})$ values for the high-redshift and low-redshift samples, together with the mean 16th and 84th percentile ranges for the low-redshift sample, are indicated in the inset of each panel.

estimates by performing a noise-degradation test using SDSS DR16Q quasar spectra (B. W. Lyke et al. 2020). We retrieved SDSS spectra of z =1–2 counterparts of our MOIRCS sample, the broad Mg II emission lines of which are clearly detected with S/N > 20 and FWHM < 5000 km s^{-1} in the DR16Q catalog. We also applied a quality cut of S/N > 15 per 300 km s^{-1} at rest-frame 3000 Å, which yields 73 objects. We artificially redshifted these spectra to $z = 6.4$ using their SDSS redshifts, and resampled both the flux and variance spectra with a 4 Å step per pixel, matching that of the MOIRCS spectra. We then degraded the spectra to S/N = 6 per 300 km s^{-1} by adding random noise, comparable to the typical quality of our MOIRCS data (Table 1). For both the original and noise-degraded spectra, we measured the Mg II line width and the continuum flux density at rest-frame 3000 Å by fitting a single Gaussian profile plus a power-law continuum model.

We find that the noise degradation introduces scatters of ±1.9% in the continuum flux density and ±19% in Mg II FWHM, while the median offsets from the original measurements are only 0.09% and 1.2%, respectively. We therefore conclude that the modest quality of the MOIRCS spectra does not introduce a significant systematic bias in the Mg II-based SMBH mass estimates. It instead adds an uncertainty of ±0.17 dex when propagated through the single-epoch $M_{\rm BH}$ recipe (Eq. 5), with the error budget dominated by the FWHM term. This additional scatter is neither large enough to explain the observed tails in the $M_{\rm BH}$ and Eddington ratio distributions relative to their mean values, nor large compared with the 0.4 dex systematic uncertainty inherent in single-epoch $M_{\rm BH}$ estimates (Y. Shen 2013).

4.4. *Impact of Single-epoch $M_{\rm BH}$ Calibration*

Single-epoch $M_{\rm BH}$ estimates rely on the $R_{\rm BLR}$–luminosity relation calibrated for local AGNs, which follows $R_{\rm BLR} \propto L_{5100}^{0.5}$ (M. C. Bentz et al. 2013). Observations have shown that high-Eddington SMBHs with $L_{\rm bol}/L_{\rm Edd} \gtrsim 1$ exhibit systematically reduced BLR sizes (i.e., shorter time lags) compared to sub-Eddington AGNs at a given luminosity (C. J. Grier et al. 2017; P. Du & J.-M. Wang 2019). A possible explanation for this trend is that the BLR size depends not only on luminosity but also on accretion physics. This effect can potentially affect current interpretations of the early growth history of SMBHs, because many of the most luminous and/or highest-redshift quasars at $z \gtrsim 6$ show high Eddington ratios (e.g., D. J. Mortlock et al. 2011; X.-B. Wu et al. 2015; E. Bañados et al. 2018; J. Yang et al. 2020; F. Wang et al. 2021).

Previous studies attempted to correct this effect using observables such as rest-frame ultraviolet Fe II emission as empirical proxies for the Eddington ratio (e.g., P. Du & J.-M. Wang 2019; Z. Pan et al. 2025). A possible dependence of single-epoch $M_{\rm BH}$ estimates on the Eddington ratio has also been discussed by E. Dalla Bontà et al. (2020). J.-H. Woo et al. (2026) recently introduced the explicit Eddington-ratio dependence into the $R_{\rm BLR}$–luminosity relation by defining a three-parameter fundamental plane. This modified single-epoch $M_{\rm BH}$ calibration minimizes the intrinsic scatter of the Hβ-based $M_{\rm BH}$ estimates to 0.21 dex.

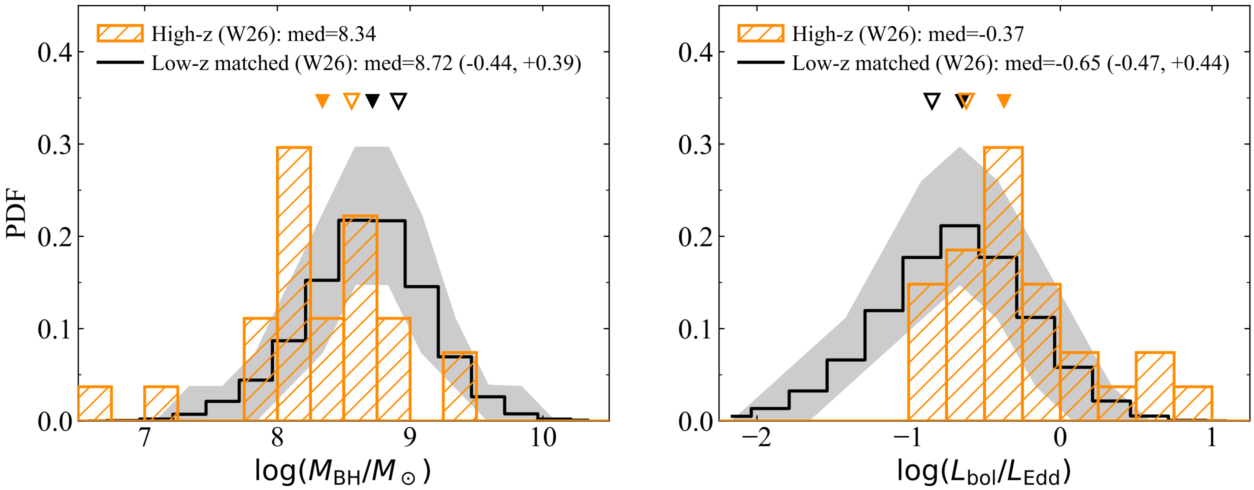

Figure 16. Same as Figure 15, but with $M_{\rm BH}$ re-estimated using the calibration of J.-H. Woo et al. (2026). The median $\log(M_{\rm BH}/M_\odot)$ and $\log(L_{\rm bol}/L_{\rm Edd})$ values in Figure 15 are indicated with open symbols to be compared with those based on the J.-H. Woo et al. (2026)'s calibration.

Figure 16 shows the $M_{\rm BH}$ and $L_{\rm bol}/L_{\rm Edd}$ distributions of our $z > 6$ sample when the J.-H. Woo et al. (2026) calibration is applied to the Hβ- and Mg II-based $M_{\rm BH}$ estimates. The distributions of the low-redshift SDSS quasars are also re-measured using the same calibration. Both the high- and low-redshift samples shift toward lower $M_{\rm BH}$ and correspondingly to higher $L_{\rm bol}/L_{\rm Edd}$. For the high-redshift sample, which has systematically higher accretion rates than the matched low-redshift quasars, the median object-by-object shifts relative to our fiducial calibration are $\Delta\log(M_{\rm BH}/M_\odot) = -0.23^{+0.05}_{-0.22}$ and $\Delta\log(L_{\rm bol}/L_{\rm Edd}) = 0.23^{+0.21}_{-0.05}$, where the quoted ranges represent the 16th–84th percentiles of the object-to-object offset distribution. The asymmetric ranges reflect the fact that the largest corrections occur for high-Eddington sources; for example, J0921+0007, J1217+0131 and J0859+0052, which have $L_{\rm bol}/L_{\rm Edd} \gtrsim 1$ under the M. Vestergaard & P. S. Osmer (2009) calibration, show the largest offsets with $\Delta\log(M_{\rm BH}/M_\odot) \simeq -0.5$ dex and $\Delta\log(L_{\rm bol}/L_{\rm Edd}) \simeq 0.5$ dex.

A notable consequence of this application is that the fraction of super-Eddington SMBHs at high redshift increases from 11% to 22%. Reflecting the stronger corrections for the higher-Eddington-ratio high-redshift quasars described above, the differences in the median BH mass and Eddington ratio between the high- and low-redshift samples also become slightly larger, with $\Delta\log(M_{\rm BH}/M_\odot)\mathrm{high-low} = -0.38$ dex and $\Delta\log(L_{\rm bol}/L_{\rm Edd})\mathrm{high-low} = 0.28$ dex, respectively, compared to -0.35 dex and 0.23 dex for the fiducial calibrations. These results are consistent with the possible importance of frequent super-Eddington episodes in the growth of distant SMBHs, as suggested by other observations (S. Collin & T. Kawaguchi 2004; T. Kawaguchi et al. 2004; F. B. Davies et al. 2019; J. Arita et al. 2023; A.-C. Eilers et al. 2024). The reduced SMBH masses and higher inferred accretion rates, if real, partly alleviate the long-standing tension between the rapid emergence of massive black holes and the short cosmic time available within the first billion years of the universe. The exact frequency and duty cycle of the super-Eddington phase in the intermediate-luminosity high-redshift quasar population will be addressed in future work, where sample completeness will be taken into account.

Finally, we note that the high fraction of super-Eddington SMBHs at high redshift is not significantly affected by the choice between Hα- and Hβ-based $M_{\rm BH}$ estimates, because the Hα-based $M_{\rm BH}$ is systematically lower than the Hβ-based estimate (Figure 13) and therefore yields a higher Eddington ratio.

5. SUMMARY

We present the results of JWST/NIRSpec and Subaru/MOIRCS near-infrared spectroscopy of 21 intermediate-luminosity quasars at $6.07 \leq z \leq 6.90$ drawn from the SHELLQs project. These SHELLQs quasars occupy the luminosity range of $\log L_{\rm bol}$ [erg s^{-1}] ~ 46–47, which lies between classical luminous $z > 6$ quasars and the faint broad-line AGN recently uncovered by JWST. The JWST/NIRSpec data from our Cycle 1 project (GO 1967) enable Balmer-line-based measurements for 12 fainter quasars beyond the sensitivity limit of ground-based spectroscopy, while the MOIRCS spectra provide Mg II-based constraints for

9 targets brighter than $M_{1450} = -24$ mag ($\approx$ 23 mag in y band). We perform single-epoch black hole mass estimates using Balmer and Mg II emission lines, and construct a $M_{\rm BH}$ sample of 27 objects combining the new data with earlier studies of the SHELLQs quasars. This large sample enables us to constrain the black hole mass and Eddington ratio distributions of $z > 6$ quasars in the intermediate-luminosity regime, $\log L_{\rm bol} \sim 46$–47.

Our main results are as follows.

1. The JWST/NIRSpec data reveal a variety of rest-frame optical emission lines in the 12 targets. Among them, two targets (J2236+0032 and J1512+4422) exhibit stellar absorption features in high-order Balmer lines, which we interpret as evidence that their host galaxies are in a post-starburst phase, as explored in detail by M. Onoue et al. (2025).

   Three targets (J1146−0005, J0844−0132, and J0217−0208) exhibit remarkably strong narrow Balmer emission lines on top of broad components. In particular, the Balmer line luminosities of J1146−0005 and J0844−0132 lie well above the local relation between the 5100 Å continuum and Balmer line luminosity, suggesting the presence of dense gas both around the nucleus and in the interstellar medium. J0217−0208 shows the weakest broad Balmer lines in our sample and may be either an AGN hosting a relatively low-mass SMBH or a star-forming galaxy with outflowing gas.

2. We detect broad Mg II emission lines in all targets observed with MOIRCS K_s-band spectroscopy. One target, J1350−0027, exhibits a double-peaked line profile, which could be interpreted either as narrow absorption at the peak of a broader emission line or as resolved Mg II doublet emission. For the other eight targets, the spectra are decomposed into an accretion-disk continuum, a pseudo-iron continuum, and Mg II emission.

3. We derive single-epoch virial black hole masses for a total of 26 SHELLQs quasars. The combined SHELLQs sample with available $M_{\rm BH}$ estimates spans $7.2 < \log(M_{\rm BH}/M_\odot) < 9.4$ and $-1.3 < \log(L_{\rm bol}/L_{\rm Edd}) < 0.4$, with a median of $\log(M_{\rm BH}/M_\odot) = 8.6$ and $\log(L_{\rm bol}/L_{\rm Edd}) = -0.63$, respectively.

4. At fixed bolometric luminosity, the $z \sim 6$ SHELLQs quasars have systematically smaller black hole masses and higher Eddington ratios than a luminosity-matched SDSS sample at $z \approx 1$–2. We find median offsets of $\Delta\log(M_{\rm BH}/M_\odot) = -0.4 \pm 0.1$ and $\Delta\log(L_{\rm bol}/L_{\rm Edd}) = +0.2 \pm 0.1$. The high-redshift sample also shows an extended tail toward the super-Eddington regime and a deficit of objects at $L_{\rm bol}/L_{\rm Edd} < 0.05$, supported by a statistical test. These results suggest that the anti-hierarchical growth of distant SMBHs extends to a representative quasar population in the epoch of cosmic reionization.

5. We test the impact of the J.-H. Woo et al. (2026) single-epoch $M_{\rm BH}$ calibration for our high-redshift sample, which accounts for the Eddington-ratio dependence of the BLR size. This calibration shifts our $z > 6$ quasars toward lower $M_{\rm BH}$ and higher $L_{\rm bol}/L_{\rm Edd}$, increasing the fraction of super-Eddington SMBHs from 11% to 22%. This result further supports the possible importance of frequent near- or super-Eddington accretion episodes in the early growth of SMBHs.

Overall, this study demonstrates that the combination of wide-field Subaru surveys and JWST spectroscopy provides a powerful route to establishing the demographic properties of SMBHs in the reionization era. Our observations reveal that a non-negligible fraction of the SHELLQs quasars are caught in a phase of rapid black hole growth, although their accretion efficiencies are less extreme than those of the most luminous quasars at similar redshifts. We will investigate the intrinsic BH mass function and Eddington ratio distribution function with selection function taken into account in our future paper (Onoue et al. in prep.). In addition, we will use the rich JWST spectral data set to investigate physical properties of the BLR and NLR gas at $z \sim 6$ in our future papers.

ACKNOWLEDGMENTS

We thank Jong-Hak Woo and his group members for valuable inputs on the black hole mass calibrations.

We thank the Subaru support astronomers for their assistance in carrying out our Subaru/MOIRCS observing programs, and Akatoki Noboriguchi and Rikako Ishimoto for their help with the observations.

This work is based on observations made with the NASA/ESA/CSA James Webb Space Telescope. The data were obtained from the Mikulski Archive for Space Telescopes at the Space Telescope Science Institute, which is operated by the Association of Universities for Research in Astronomy, Inc., under NASA contract NAS 5-03127 for JWST. These observations are associated with programs GO #1967. Support for these programs was provided by NASA through a grant from the Space Telescope Science Institute (JWST-GO-01967.002-A), which is operated by the Association of Universities for Research in Astronomy, Inc., under NASA contract NAS 5-03127. This work was supported by World Premier International Research Center Initiative (WPI), MEXT, Japan. This work used computing resources at Kavli IPMU.

M.O., Y.M., M.I., K.K., T.K., N.K., T.N., and T.I. acknowledge support from JSPS KAKENHI Grant Numbers 24K22894, 26K07155, 21H04494, 26K00745, JP25K07359, JP23K20035, JP24H00004, JP25K07370, JP25H00663, JP25K01038, JP25K01044, JP23K25911, and JP25H00671. K.Inayoshi acknowledges support from the National Natural Science Foundation of China (12573015, W2532003), the Beijing Natural Science Foundation (IS25003), and the China Manned Space Program (CMS-CSST-2025-A09). K.Iwasawa acknowledges support under the grant PID2022-136828NB-C44 provided by MCIN/AEI/10.13039/501100011033 / FEDER, UE. M.Sawamura is supported by JST SPRING, Grant Number JPMJSP2108. This paper is a part of the outcome of research performed under a Waseda University Grant for Special Research Projects (Project number: 2025R-062).

Facilities: JWST (NIRSpec), Subaru (MOIRCS)

Software: astropy (Astropy Collaboration et al. 2013), matplotlib (J. D. Hunter 2007), scipy (P. Virtanen et al. 2020), IRAF (D. Tody 1986), QSOFitMORE (Y. Fu 2021)

APPENDIX

A. BLACK HOLE MASSES BASED ON TSUZUKI ET AL. IRON TEMPLATE

Here, we present in Table 7 the Mg II line profiles of the MOIRCS targets obtained using the Y. Tsuzuki et al. (2006) iron template, which better represents the iron emission underlying the Mg II line than the M. Vestergaard & B. J. Wilkes (2001) template. The format of the table is the same as in Table 5.

Table 7. Mg II profiles (Y. Tsuzuki et al. 2006 iron template)

ID	$z_{\rm MgII}$	L_{3000}	FWHM(Mg II)	$L_{\rm MgII}$
		[10^{45} erg s^{-1}]	[km s^{-1}]	[10^{43} erg s^{-1}]
J2210+0304	$6.861^{+0.006}_{-0.005}$	4.7 ± 0.4	3900^{+900}_{-1000}	$4.4^{+0.6}_{-0.8}$
J0921+0007	$6.563^{+0.001}_{-0.001}$	14.3 ± 0.6	1700^{+100}_{-100}	$11.3^{+0.7}_{-0.7}$
J1545+4232	$6.514^{+0.002}_{-0.002}$	4.5 ± 0.3	2900^{+200}_{-200}	$7.5^{+0.4}_{-0.4}$
J1004+0239	$6.403^{+0.003}_{-0.003}$	3.7 ± 0.2	2400^{+900}_{-500}	$4.2^{+0.6}_{-0.5}$
J1137+0045	$6.361^{+0.003}_{-0.003}$	2.7 ± 0.2	4600^{+200}_{-400}	$5.7^{+0.5}_{-0.4}$
J2304+0045	$6.336^{+0.004}_{-0.003}$	2.3 ± 0.1	2900^{+400}_{-400}	$3.1^{+0.5}_{-0.3}$
J1406−0116	$6.292^{+0.003}_{-0.002}$	3.5 ± 0.2	2500^{+200}_{-200}	$2.7^{+0.2}_{-0.2}$
J1217+0131	$6.205^{+0.004}_{-0.004}$	11.5 ± 0.3	2000^{+100}_{-300}	$5.4^{+0.9}_{-0.8}$

B. FULL TABLE FOR THE JWST LINE MEASUREMENTS

Here, we provide the full set of parameters derived from the continuum+line fitting of the JWST/NIRSpec G395M spectra of the 12 targets in machine-readable form. Because of the large number of columns, Table 8 provides a description of each column rather than displaying the individual measurements. The complete table is provided as ancillary material with this manuscript.

Table 8. Description of the Machine-readable Table of the JWST Spectral Measurements

Column	Label	Unit	Description
1	`ID`	···	Object identifier
2	`redshift`	···	Best-fit [O III] redshift
3	`redshift_err`	···	Uncertainty in the [O III] redshift
4	`ra`	deg	Right ascension
5	`dec`	deg	Declination
6	`PL_norm`	10^{-17}erg cm^{-2} s^{-1} Å^{-1}	Normalization of the power-law continuum at rest-frame 3000 Å
7	`PL_norm_err`	10^{-17}erg cm^{-2} s^{-1} Å^{-1}	Uncertainty in the power-law normalization
8	`PL_slope`	···	Slope of the power-law continuum
9	`PL_slope_err`	···	Uncertainty in the power-law slope
10	`L_Fe_w3980_w4040`	10^{42} erg s^{-1}	Integrated Fe II luminosity over 3980–4040 Å
11	`L_Fe_w3980_w4040_err`	10^{42} erg s^{-1}	Uncertainty in the integrated Fe II luminosity over 3980–4040 Å
12	`L_Fe_w4435_w4685`	10^{42} erg s^{-1}	Integrated Fe II luminosity over 4435–4685 Å
13	`L_Fe_w4435_w4685_err`	10^{42} erg s^{-1}	Uncertainty in the integrated Fe II luminosity over 4435–4685 Å
14	`L_Fe_w5100_w5500`	10^{42} erg s^{-1}	Integrated Fe II luminosity over 5100–5500 Å
15	`L_Fe_w5100_w5500_err`	10^{42} erg s^{-1}	Uncertainty in the integrated Fe II luminosity over 5100–5500 Å
16	`L_Ha_broad`	10^{42} erg s^{-1}	Luminosity of the broad Hα component
17	`L_Ha_broad_err`	10^{42} erg s^{-1}	Uncertainty in the luminosity of the broad Hα component
18	`L_Hb_broad`	10^{42} erg s^{-1}	Luminosity of the broad Hβ component
19	`L_Hb_broad_err`	10^{42} erg s^{-1}	Uncertainty in the luminosity of the broad Hβ component
20	`L_Hg_broad`	10^{42} erg s^{-1}	Luminosity of the broad Hγ component
21	`L_Hg_broad_err`	10^{42} erg s^{-1}	Uncertainty in the luminosity of the broad Hγ component
22	`L_Hd_broad`	10^{42} erg s^{-1}	Luminosity of the broad Hδ component
23	`L_Hd_broad_err`	10^{42} erg s^{-1}	Uncertainty in the luminosity of the broad Hδ component
24	`L_Ha_narrow`	10^{42} erg s^{-1}	Luminosity of the narrow Hα component
25	`L_Ha_narrow_err`	10^{42} erg s^{-1}	Uncertainty in the luminosity of the narrow Hα component
26	`L_Hb_narrow`	10^{42} erg s^{-1}	Luminosity of the narrow Hβ component
27	`L_Hb_narrow_err`	10^{42} erg s^{-1}	Uncertainty in the luminosity of the narrow Hβ component
28	`L_Hg_narrow`	10^{42} erg s^{-1}	Luminosity of the narrow Hγ component
29	`L_Hg_narrow_err`	10^{42} erg s^{-1}	Uncertainty in the luminosity of the narrow Hγ component
30	`L_Hd_narrow`	10^{42} erg s^{-1}	Luminosity of the narrow Hδ component
31	`L_Hd_narrow_err`	10^{42} erg s^{-1}	Uncertainty in the luminosity of the narrow Hδ component
32	`L_O3_5007_c`	10^{42} erg s^{-1}	Luminosity of the core [O III] λ5007 component
33	`L_O3_5007_c_err`	10^{42} erg s^{-1}	Uncertainty in the luminosity of the core [O III] λ5007 component
34	`L_O3_5007_w`	10^{42} erg s^{-1}	Luminosity of the wing [O III] λ5007 component

Table 8 *continued*

Table 8 *(continued)*

Column	Label	Unit	Description
35	L_O3_5007_w_err	10^{42} erg s^{-1}	Uncertainty in the luminosity of the wing [O III] λ5007 component
36	L_O3_4959_c	10^{42} erg s^{-1}	Luminosity of the core [O III] λ4959 component
37	L_O3_4959_c_err	10^{42} erg s^{-1}	Uncertainty in the luminosity of the core [O III] λ4959 component
38	L_O3_4959_w	10^{42} erg s^{-1}	Luminosity of the wing [O III] λ4959 component
39	L_O3_4959_w_err	10^{42} erg s^{-1}	Uncertainty in the luminosity of the wing [O III] λ4959 component
40	L_N2_6585	10^{42} erg s^{-1}	Luminosity of [N II] λ6585
41	L_N2_6585_err	10^{42} erg s^{-1}	Uncertainty in the luminosity of [N II] λ6585
42	FWHM_Ha_broad	km s^{-1}	FWHM of the broad Hα component
43	FWHM_Ha_broad_err	km s^{-1}	Uncertainty in the FWHM of the broad Hα component
44	FWHM_Hb_broad	km s^{-1}	FWHM of the broad Hβ component
45	FWHM_Hb_broad_err	km s^{-1}	Uncertainty in the FWHM of the broad Hβ component
46	FWHM_Hg_broad	km s^{-1}	FWHM of the broad Hγ component
47	FWHM_Hg_broad_err	km s^{-1}	Uncertainty in the FWHM of the broad Hγ component
48	FWHM_Hd_broad	km s^{-1}	FWHM of the broad Hδ component
49	FWHM_Hd_broad_err	km s^{-1}	Uncertainty in the FWHM of the broad Hδ component
50	FWHM_Ha_narrow	km s^{-1}	FWHM of the narrow Hα component
51	FWHM_Ha_narrow_err	km s^{-1}	Uncertainty in the FWHM of the narrow Hα component
52	FWHM_Hb_narrow	km s^{-1}	FWHM of the narrow Hβ component
53	FWHM_Hb_narrow_err	km s^{-1}	Uncertainty in the FWHM of the narrow Hβ component
54	FWHM_Hg_narrow	km s^{-1}	FWHM of the narrow Hγ component
55	FWHM_Hg_narrow_err	km s^{-1}	Uncertainty in the FWHM of the narrow Hγ component
56	FWHM_Hd_narrow	km s^{-1}	FWHM of the narrow Hδ component
57	FWHM_Hd_narrow_err	km s^{-1}	Uncertainty in the FWHM of the narrow Hδ component
58	FWHM_O3_5007_c	km s^{-1}	FWHM of the core [O III] λ5007 component
59	FWHM_O3_5007_c_err	km s^{-1}	Uncertainty in the FWHM of the core [O III] λ5007 component
60	FWHM_O3_5007_w	km s^{-1}	FWHM of the wing [O III] λ5007 component
61	FWHM_O3_5007_w_err	km s^{-1}	Uncertainty in the FWHM of the wing [O III] λ5007 component
62	FWHM_O3_4959_c	km s^{-1}	FWHM of the core [O III] λ4959 component
63	FWHM_O3_4959_c_err	km s^{-1}	Uncertainty in the FWHM of the core [O III] λ4959 component
64	FWHM_O3_4959_w	km s^{-1}	FWHM of the wing [O III] λ4959 component
65	FWHM_O3_4959_w_err	km s^{-1}	Uncertainty in the FWHM of the wing [O III] λ4959 component

NOTE— The complete table is provided in machine-readable form as ancillary material with this manuscript. For [O III], the suffixes “c” and “w” denote the core and wing components, respectively.

REFERENCES

Aihara, H., Arimoto, N., Armstrong, R., et al. 2018, Publications of the Astronomical Society of Japan, 70, S4, doi: 10.1093/pasj/psx066

Aihara, H., AlSayyad, Y., Ando, M., et al. 2022, PASJ, 74, 247, doi: 10.1093/pasj/psab122

Anderson, T. W., & Darling, D. A. 1952, The Annals of Mathematical Statistics, 23, 193, doi: 10.1214/aoms/1177729437

Arita, J., Kashikawa, N., Matsuoka, Y., et al. 2023, ApJ, 954, 210, doi: 10.3847/1538-4357/ace43a

Astropy Collaboration, Robitaille, T. P., Tollerud, E. J., et al. 2013, A&A, 558, A33, doi: 10.1051/0004-6361/201322068

Bañados, E., Venemans, B. P., Decarli, R., et al. 2016, ApJS, 227, 11, doi: 10.3847/0067-0049/227/1/11

Bañados, E., Venemans, B. P., Mazzucchelli, C., et al. 2018, Nature, 553, 473, doi: 10.1038/nature25180

Bañados, E., Mazzucchelli, C., Momjian, E., et al. 2021, ApJ, 909, 80, doi: 10.3847/1538-4357/abe239

Bañados, E., Le Brun, V., Belladitta, S., et al. 2025, MNRAS, 542, 1088, doi: 10.1093/mnras/staf1274

Bentz, M. C., Walsh, J. L., Barth, A. J., et al. 2010, ApJ, 716, 993, doi: 10.1088/0004-637X/716/2/993

Bentz, M. C., Denney, K. D., Grier, C. J., et al. 2013, ApJ, 767, 149, doi: 10.1088/0004-637X/767/2/149

Boroson, T. A., & Green, R. F. 1992, ApJS, 80, 109, doi: 10.1086/191661

Brammer, G. 2023, msaexp: NIRSpec analyis tools, 0.6.17 Zenodo, doi: 10.5281/zenodo.8319596

Choi, H., Leighly, K. M., Terndrup, D. M., et al. 2022, ApJ, 937, 74, doi: 10.3847/1538-4357/ac61d9

Collin, S., & Kawaguchi, T. 2004, A&A, 426, 797, doi: 10.1051/0004-6361:20040528

Dalla Bontà, E., Peterson, B. M., Bentz, M. C., et al. 2020, ApJ, 903, 112, doi: 10.3847/1538-4357/abbc1c

Davies, F. B., Hennawi, J. F., & Eilers, A.-C. 2019, ApJL, 884, L19, doi: 10.3847/2041-8213/ab42e3

de Graaff, A., Rix, H.-W., Naidu, R. P., et al. 2025, A&A, 701, A168, doi: 10.1051/0004-6361/202554681

de Graaff, A., Hviding, R. E., Naidu, R. P., et al. 2026, MNRAS, doi: 10.1093/mnras/stag1567

Ding, X., Onoue, M., Silverman, J. D., et al. 2023, Nature, 621, 51, doi: 10.1038/s41586-023-06345-5

Ding, X., Onoue, M., Silverman, J. D., et al. 2025, ApJ, 993, 91, doi: 10.3847/1538-4357/ae045b

Du, P., & Wang, J.-M. 2019, ApJ, 886, 42, doi: 10.3847/1538-4357/ab4908

Ebizuka, N., Ichiyama, K., Yamada, T., et al. 2011, PASJ, 63, 605, doi: 10.1093/pasj/63.sp2.S605

Eilers, A.-C., Simcoe, R. A., Yue, M., et al. 2023, ApJ, 950, 68, doi: 10.3847/1538-4357/acd776

Eilers, A.-C., Mackenzie, R., Pizzati, E., et al. 2024, ApJ, 974, 275, doi: 10.3847/1538-4357/ad778b

Eracleous, M., Lewis, K. T., & Flohic, H. M. L. G. 2009, NewAR, 53, 133, doi: 10.1016/j.newar.2009.07.005

Euclid Collaboration, Barnett, R., Warren, S. J., et al. 2019, A&A, 631, A85, doi: 10.1051/0004-6361/201936427

Fabricius, M., Walawender, J., Arimoto, N., et al. 2016, in Society of Photo-Optical Instrumentation Engineers (SPIE) Conference Series, Vol. 9908, Ground-based and Airborne Instrumentation for Astronomy VI, ed. C. J. Evans, L. Simard, & H. Takami, 990828, doi: 10.1117/12.2231417

Fan, X., Bañados, E., & Simcoe, R. A. 2023, ARA&A, 61, 373, doi: 10.1146/annurev-astro-052920-102455

Farina, E. P., Schindler, J.-T., Walter, F., et al. 2022, ApJ, 941, 106, doi: 10.3847/1538-4357/ac9626

Fu, Y. 2021, QSOFITMORE: a python package for fitting UV-optical spectra of quasars, v1.1.0 Zenodo, doi: 10.5281/zenodo.5810042

Genzel, R., Eisenhauer, F., & Gillessen, S. 2010, Reviews of Modern Physics, 82, 3121, doi: 10.1103/RevModPhys.82.3121

Ghez, A. M., Salim, S., Weinberg, N. N., et al. 2008, ApJ, 689, 1044, doi: 10.1086/592738

GRAVITY+ Collaboration, Abd El Dayem, K., Aimar, N., et al. 2026, A&A, 706, A99, doi: 10.1051/0004-6361/202557285

Greene, J. E., & Ho, L. C. 2005, ApJ, 630, 122, doi: 10.1086/431897

Greene, J. E., Labbe, I., Goulding, A. D., et al. 2024, ApJ, 964, 39, doi: 10.3847/1538-4357/ad1e5f

Greene, J. E., Setton, D. J., Furtak, L. J., et al. 2026, ApJ, 996, 129, doi: 10.3847/1538-4357/ae1836

Grier, C. J., Trump, J. R., Shen, Y., et al. 2017, ApJ, 851, 21, doi: 10.3847/1538-4357/aa98dc

Guo, H., Shen, Y., & Wang, S. 2018, PyQSOFit: Python code to fit the spectrum of quasars,, Astrophysics Source Code Library, record ascl:1809.008

Hall, P. B., Anderson, S. F., Strauss, M. A., et al. 2002, ApJS, 141, 267, doi: 10.1086/340546

Halpern, J. P., & Steiner, J. E. 1983, ApJL, 269, L37, doi: 10.1086/184051

Harikane, Y., Zhang, Y., Nakajima, K., et al. 2023, ApJ, 959, 39, doi: 10.3847/1538-4357/ad029e

Hopkins, P. F., Strauss, M. A., Hall, P. B., et al. 2004, AJ, 128, 1112, doi: 10.1086/423291

Hunter, J. D. 2007, Computing in Science & Engineering, 9, 90, doi: 10.1109/MCSE.2007.55

Ichikawa, T., Suzuki, R., Tokoku, C., et al. 2006, in Society of Photo-Optical Instrumentation Engineers (SPIE) Conference Series, Vol. 6269, Society of Photo-Optical Instrumentation Engineers (SPIE) Conference Series, ed. I. S. McLean & M. Iye, 626916, doi: 10.1117/12.670078

Inayoshi, K., & Maiolino, R. 2025, ApJL, 980, L27, doi: 10.3847/2041-8213/adaebd

Inayoshi, K., Visbal, E., & Haiman, Z. 2020, ARA&A, 58, 27, doi: 10.1146/annurev-astro-120419-014455
Ishimoto, R., Kashikawa, N., Onoue, M., et al. 2020, ApJ, 903, 60, doi: 10.3847/1538-4357/abb80b
Ivezić, Ž., Kahn, S. M., Tyson, J. A., et al. 2019, ApJ, 873, 111, doi: 10.3847/1538-4357/ab042c
Jakobsen, P., Ferruit, P., Alves de Oliveira, C., et al. 2022, A&A, 661, A80, doi: 10.1051/0004-6361/202142663
Jiang, L., Fan, X., Vestergaard, M., et al. 2007, AJ, 134, 1150, doi: 10.1086/520811
Juodžbalis, I., Maiolino, R., Baker, W. M., et al. 2026, MNRAS, 546, stag086, doi: 10.1093/mnras/stag086
Kashikawa, N., Ishizaki, Y., Willott, C. J., et al. 2015, ApJ, 798, 28, doi: 10.1088/0004-637X/798/1/28
Kaspi, S., Smith, P. S., Netzer, H., et al. 2000, ApJ, 533, 631, doi: 10.1086/308704
Kato, N., Matsuoka, Y., Onoue, M., et al. 2020, PASJ, 72, 84, doi: 10.1093/pasj/psaa074
Kawaguchi, T., Aoki, K., Ohta, K., & Collin, S. 2004, A&A, 420, L23, doi: 10.1051/0004-6361:20040157
Kido, D., Ioka, K., Hotokezaka, K., Inayoshi, K., & Irwin, C. M. 2025, MNRAS, 544, 3407, doi: 10.1093/mnras/staf1898
Kim, Y., Im, M., Jeon, Y., et al. 2018, ApJ, 855, 138, doi: 10.3847/1538-4357/aaadae
Kocevski, D. D., Onoue, M., Inayoshi, K., et al. 2023, ApJL, 954, L4, doi: 10.3847/2041-8213/ace5a0
Kocevski, D. D., Finkelstein, S. L., Barro, G., et al. 2025, ApJ, 986, 126, doi: 10.3847/1538-4357/adbc7d
Kurk, J. D., Walter, F., Fan, X., et al. 2007, ApJ, 669, 32, doi: 10.1086/521596
La Mura, G., Popović, L. Č., Ciroi, S., Rafanelli, P., & Ilić, D. 2007, ApJ, 671, 104, doi: 10.1086/522821
Leggett, S. K., Currie, M. J., Varricatt, W. P., et al. 2006, MNRAS, 373, 781, doi: 10.1111/j.1365-2966.2006.11069.x
Li, W., Inayoshi, K., Onoue, M., & Toyouchi, D. 2023, ApJ, 950, 85, doi: 10.3847/1538-4357/accbbe
Liu, W., Farina, E. P., Fan, X., et al. 2026, arXiv e-prints, arXiv:2606.03037, doi: 10.48550/arXiv.2606.03037
Lupi, A., Quadri, G., Volonteri, M., Colpi, M., & Regan, J. A. 2024, A&A, 686, A256, doi: 10.1051/0004-6361/202348788
Lyke, B. W., Higley, A. N., McLane, J. N., et al. 2020, ApJS, 250, 8, doi: 10.3847/1538-4365/aba623
Lyu, J., Rieke, G. H., Stone, M., et al. 2025, ApJL, 981, L20, doi: 10.3847/2041-8213/adb613
Madau, P., Haardt, F., & Dotti, M. 2014, ApJL, 784, L38, doi: 10.1088/2041-8205/784/2/L38
Maiolino, R., Scholtz, J., Curtis-Lake, E., et al. 2024, A&A, 691, A145, doi: 10.1051/0004-6361/202347640
Markov, V., Gallerani, S., Ferrara, A., et al. 2025, Nature Astronomy, 9, 458, doi: 10.1038/s41550-024-02426-1
Marques-Chaves, R., Schaerer, D., Dessauges-Zavadsky, M., et al. 2025, arXiv e-prints, arXiv:2510.12411, doi: 10.48550/arXiv.2510.12411
Matsuoka, Y., Onoue, M., Kashikawa, N., et al. 2016, ApJ, 828, 26, doi: 10.3847/0004-637X/828/1/26
Matsuoka, Y., Onoue, M., Kashikawa, N., et al. 2018a, Publications of the Astronomical Society of Japan, 70, S35, doi: 10.1093/pasj/psx046
Matsuoka, Y., Iwasawa, K., Onoue, M., et al. 2018b, The Astrophysical Journal Supplement Series, 237, 5, doi: 10.3847/1538-4365/aac724
Matsuoka, Y., Strauss, M. A., Kashikawa, N., et al. 2018c, ApJ, 869, 150, doi: 10.3847/1538-4357/aaee7a
Matsuoka, Y., Onoue, M., Kashikawa, N., et al. 2019a, ApJ, 872, L2, doi: 10.3847/2041-8213/ab0216
Matsuoka, Y., Iwasawa, K., Onoue, M., et al. 2019b, ApJ, 883, 183, doi: 10.3847/1538-4357/ab3c60
Matsuoka, Y., Iwasawa, K., Onoue, M., et al. 2022, ApJS, 259, 18, doi: 10.3847/1538-4365/ac3d31
Matsuoka, Y., Izumi, T., Onoue, M., et al. 2024, ApJL, 965, L4, doi: 10.3847/2041-8213/ad35c7
Matsuoka, Y., Onoue, M., Iwasawa, K., et al. 2025a, ApJ, 988, 57, doi: 10.3847/1538-4357/addf4e
Matsuoka, Y., Iwasawa, K., Onoue, M., et al. 2025b, ApJS, 280, 68, doi: 10.3847/1538-4365/ae0035
Matthee, J., Naidu, R. P., Brammer, G., et al. 2024, ApJ, 963, 129, doi: 10.3847/1538-4357/ad2345
Mazzucchelli, C., Bañados, E., Venemans, B. P., et al. 2017, ApJ, 849, 91, doi: 10.3847/1538-4357/aa9185
Mazzucchelli, C., Bischetti, M., D'Odorico, V., et al. 2023, A&A, 676, A71, doi: 10.1051/0004-6361/202346317
Mejía-Restrepo, J. E., Trakhtenbrot, B., Koss, M. J., et al. 2022, ApJS, 261, 5, doi: 10.3847/1538-4365/ac6602
Merloni, A. 2004, MNRAS, 353, 1035, doi: 10.1111/j.1365-2966.2004.08147.x
Miyazaki, S., Komiyama, Y., Kawanomoto, S., et al. 2018, Publications of the Astronomical Society of Japan, 70, S1, doi: 10.1093/pasj/psx063
Mortlock, D. J., Warren, S. J., Venemans, B. P., et al. 2011, Nature, 474, 616, doi: 10.1038/nature10159
Naidu, R. P., Matthee, J., Katz, H., et al. 2025, arXiv e-prints, arXiv:2503.16596, doi: 10.48550/arXiv.2503.16596
Nanni, R., Vignali, C., Gilli, R., Moretti, A., & Brandt, W. N. 2017, A&A, 603, A128, doi: 10.1051/0004-6361/201730484
Netzer, H., Lira, P., Trakhtenbrot, B., Shemmer, O., & Cury, I. 2007, ApJ, 671, 1256, doi: 10.1086/523035

Ni, Y., Di Matteo, T., Gilli, R., et al. 2020, MNRAS, 495, 2135, doi: 10.1093/mnras/staa1313
Oke, J. B., & Gunn, J. E. 1983, ApJ, 266, 713, doi: 10.1086/160817
Onoue, M., Kashikawa, N., Willott, C. J., et al. 2017, ApJ, 847, L15, doi: 10.3847/2041-8213/aa8cc6
Onoue, M., Kashikawa, N., Matsuoka, Y., et al. 2019, ApJ, 880, 77, doi: 10.3847/1538-4357/ab29e9
Onoue, M., Bañados, E., Mazzucchelli, C., et al. 2020, ApJ, 898, 105, doi: 10.3847/1538-4357/aba193
Onoue, M., Matsuoka, Y., Kashikawa, N., et al. 2021, ApJ, 919, 61, doi: 10.3847/1538-4357/ac0f07
Onoue, M., Inayoshi, K., Ding, X., et al. 2023, ApJL, 942, L17, doi: 10.3847/2041-8213/aca9d3
Onoue, M., Ding, X., Silverman, J. D., et al. 2025, Nature Astronomy, 9, 1541, doi: 10.1038/s41550-025-02628-1
Osterbrock, D. E., & Ferland, G. J. 2006, Astrophysics of gaseous nebulae and active galactic nuclei
Pan, Z., Jiang, L., Guo, W.-J., et al. 2025, ApJ, 987, 48, doi: 10.3847/1538-4357/add7dd
Pâris, I., Petitjean, P., Aubourg, É., et al. 2018, A&A, 613, A51, doi: 10.1051/0004-6361/201732445
Pei, Y. C. 1992, ApJ, 395, 130, doi: 10.1086/171637
Phillips, C. L., Strauss, M. A., Onoue, M., et al. 2026, ApJ, 1003, 47, doi: 10.3847/1538-4357/ae606d
Richards, G. T., Hall, P. B., Vand en Berk, D. E., et al. 2003, AJ, 126, 1131, doi: 10.1086/377014
Richards, G. T., Lacy, M., Storrie-Lombardi, L. J., et al. 2006, The Astrophysical Journal Supplement Series, 166, 470, doi: 10.1086/506525
Rigby, J., Perrin, M., McElwain, M., et al. 2023, PASP, 135, 048001, doi: 10.1088/1538-3873/acb293
Sameshima, H., Yoshii, Y., & Kawara, K. 2017, ApJ, 834, 203, doi: 10.3847/1538-4357/834/2/203
Schindler, J.-T., Farina, E. P., Bañados, E., et al. 2020, ApJ, 905, 51, doi: 10.3847/1538-4357/abc2d7
Schlegel, D. J., Finkbeiner, D. P., & Davis, M. 1998, ApJ, 500, 525, doi: 10.1086/305772
Schulze, A., & Wisotzki, L. 2010, A&A, 516, A87, doi: 10.1051/0004-6361/201014193
Schulze, A., Silverman, J. D., Kashino, D., et al. 2018, ApJS, 239, 22, doi: 10.3847/1538-4365/aae82f
Schwarz, G. 1978, Annals of Statistics, 6, 461
Selsing, J., Fynbo, J. P. U., Christensen, L., & Krogager, J. K. 2016, A&A, 585, A87, doi: 10.1051/0004-6361/201527096
Shemmer, O., Netzer, H., Maiolino, R., et al. 2004, ApJ, 614, 547, doi: 10.1086/423607
Shen, Y. 2013, Bulletin of the Astronomical Society of India, 41, 61. https://arxiv.org/abs/1302.2643
Shen, Y., Richards, G. T., Strauss, M. A., et al. 2011, The Astrophysical Journal Supplement Series, 194, 45, doi: 10.1088/0067-0049/194/2/45
Shen, Y., Wu, J., Jiang, L., et al. 2019, ApJ, 873, 35, doi: 10.3847/1538-4357/ab03d9
Shen, Y., Grier, C. J., Horne, K., et al. 2024, ApJS, 272, 26, doi: 10.3847/1538-4365/ad3936
Shirakata, H., Kawaguchi, T., Oogi, T., Okamoto, T., & Nagashima, M. 2019, MNRAS, 487, 409, doi: 10.1093/mnras/stz1282
Silverman, J. D., Li, J., Ding, X., et al. 2025, ApJL, 995, L67, doi: 10.3847/2041-8213/ae279c
Son, S., Kim, M., Ho, L. C., & Li, R. 2025, ApJ, 995, 37, doi: 10.3847/1538-4357/ae1ef1
Suzuki, R., Tokoku, C., Ichikawa, T., et al. 2008, PASJ, 60, 1347, doi: 10.1093/pasj/60.6.1347
Takahashi, A., Matsuoka, Y., Onoue, M., et al. 2024, ApJ, 960, 112, doi: 10.3847/1538-4357/ad045e
Taylor, A. J., Kokorev, V., Kocevski, D. D., et al. 2025, ApJL, 989, L7, doi: 10.3847/2041-8213/ade789
Tee, W. L., Fan, X., Wang, F., et al. 2023, ApJ, 956, 52, doi: 10.3847/1538-4357/acf12d
Tody, D. 1986, in Society of Photo-Optical Instrumentation Engineers (SPIE) Conference Series, Vol. 627, Instrumentation in astronomy VI, ed. D. L. Crawford, 733, doi: 10.1117/12.968154
Trakhtenbrot, B., Volonteri, M., & Natarajan, P. 2017, ApJL, 836, L1, doi: 10.3847/2041-8213/836/1/L1
Tsuzuki, Y., Kawara, K., Yoshii, Y., et al. 2006, ApJ, 650, 57, doi: 10.1086/506376
Ueda, Y., Akiyama, M., Ohta, K., & Miyaji, T. 2003, ApJ, 598, 886, doi: 10.1086/378940
Umeda, H., Inayoshi, K., Harikane, Y., & Murase, K. 2025, arXiv e-prints, arXiv:2512.04208, doi: 10.48550/arXiv.2512.04208
Vanden Berk, D. E., Richards, G. T., Bauer, A., et al. 2001, AJ, 122, 549, doi: 10.1086/321167
Vestergaard, M. 2002, ApJ, 571, 733, doi: 10.1086/340045
Vestergaard, M., & Osmer, P. S. 2009, ApJ, 699, 800, doi: 10.1088/0004-637X/699/1/800
Vestergaard, M., & Peterson, B. M. 2006, ApJ, 641, 689, doi: 10.1086/500572
Vestergaard, M., & Wilkes, B. J. 2001, The Astrophysical Journal Supplement Series, 134, 1, doi: 10.1086/320357
Virtanen, P., Gommers, R., Oliphant, T. E., et al. 2020, Nature Methods, 17, 261, doi: 10.1038/s41592-019-0686-2
Vito, F., Brandt, W. N., Yang, G., et al. 2018, MNRAS, 473, 2378, doi: 10.1093/mnras/stx2486
Volonteri, M., Silk, J., & Dubus, G. 2015, ApJ, 804, 148, doi: 10.1088/0004-637X/804/2/148

Walawender, J., Wung, M., Fabricius, M., et al. 2016, in Society of Photo-Optical Instrumentation Engineers (SPIE) Conference Series, Vol. 9908, Ground-based and Airborne Instrumentation for Astronomy VI, ed. C. J. Evans, L. Simard, & H. Takami, 99082G, doi: 10.1117/12.2231812

Wang, F., Fan, X., Yang, J., et al. 2017, ApJ, 839, 27, doi: 10.3847/1538-4357/aa689f

Wang, F., Yang, J., Fan, X., et al. 2021, ApJL, 907, L1, doi: 10.3847/2041-8213/abd8c6

Wang, F., Yang, J., Hennawi, J. F., et al. 2023, ApJL, 951, L4, doi: 10.3847/2041-8213/accd6f

Wang, F., Yang, J., Fan, X., et al. 2024, ApJ, 968, 9, doi: 10.3847/1538-4357/ad3fb4

Wang, F., Champagne, J. B., Huang, J., et al. 2026, arXiv e-prints, arXiv:2602.04979, doi: 10.48550/arXiv.2602.04979

Ward, C., Gezari, S., Nugent, P., et al. 2024, ApJ, 961, 172, doi: 10.3847/1538-4357/ad147d

Willott, C. J., Albert, L., Arzoumanian, D., et al. 2010, AJ, 140, 546, doi: 10.1088/0004-6256/140/2/546

Wolf, J., Nandra, K., Salvato, M., et al. 2023, A&A, 669, A127, doi: 10.1051/0004-6361/202244688

Woo, J.-H., Kim, J., Cho, H., & Wang, S. 2026, ApJ, 1003, 123, doi: 10.3847/1538-4357/ae6109

Woo, J.-H., Le, H. A. N., Karouzos, M., et al. 2018, ApJ, 859, 138, doi: 10.3847/1538-4357/aabf3e

Woo, J.-H., Yoon, Y., Park, S., Park, D., & Kim, S. C. 2015, ApJ, 801, 38, doi: 10.1088/0004-637X/801/1/38

Wu, Q., & Shen, Y. 2022, ApJS, 263, 42, doi: 10.3847/1538-4365/ac9ead

Wu, X.-B., Wang, F., Fan, X., et al. 2015, Nature, 518, 512, doi: 10.1038/nature14241

Yan, Z., Inayoshi, K., Chen, K., & Guo, J. 2025, arXiv e-prints, arXiv:2512.11050, doi: 10.48550/arXiv.2512.11050

Yang, D., Hennawi, J. F., Guarneri, F., et al. 2026, A&A, 711, A104, doi: 10.1051/0004-6361/202658883

Yang, J., Wang, F., Fan, X., et al. 2020, ApJL, 897, L14, doi: 10.3847/2041-8213/ab9c26

Yang, J., Wang, F., Fan, X., et al. 2021, ApJ, 923, 262, doi: 10.3847/1538-4357/ac2b32

Yang, J., Wang, F., Fan, X., et al. 2023, ApJL, 951, L5, doi: 10.3847/2041-8213/acc9c8

Yue, M., Eilers, A.-C., Simcoe, R. A., et al. 2024, ApJ, 966, 176, doi: 10.3847/1538-4357/ad3914